

Effects of seasonal variations in vegetation and precipitation on catchment erosion rates along a climate and ecological gradient: Insights from numerical modelling

Hemanti Sharma¹ and Todd A. Ehlers^{2,1}

¹Department of Geosciences, University of Tübingen, Schnarrenbergstr. 94-96, 72076, Germany

²School of Geographical and Earth Sciences, University of Glasgow, Glasgow, Scotland

Correspondence to: Todd A. Ehlers (todd.ehlers@glasgow.ac.uk)

Abstract. Precipitation in wet seasons influences catchment erosion and contributes to annual erosion rates. However, wet seasons are also associated with increased vegetation cover, which helps resist erosion. This study investigates the effect of present-day seasonal variations in rainfall and vegetation cover on erosion rates for four catchments along the extreme climate and ecological gradient (from arid to temperate) of the Chilean Coastal Cordillera (~26 °S – ~38 °S). We do this using the Landlab-SPACE landscape evolution model to account for vegetation-dependent hillslope-fluvial processes and hillslope hydrology. Model inputs include present-day (90 m) topography, and a timeseries (from 2000-2019) of MODIS-derived NDVI for vegetation seasonality; weather station observations of precipitation; and evapotranspiration obtained from GLDAS NOAH. The sensitivity of catchment scale erosion rates to seasonal average variations in precipitation and/or vegetation cover was quantified using numerical model simulations. Simulations were conducted for 1,000 years (20 years of vegetation and precipitation observations repeated 50 times). After detrending the results for long-term transient changes, the last 20 years were analyzed. Results indicate that when vegetation cover is variable but precipitation is held constant, the amplitude of change in erosion rates relative to mean erosion rates ranges between 5% (arid) to 36% (Mediterranean setting). In contrast, in simulations with variable precipitation change and constant vegetation cover, the amplitude of change in erosion rates is higher and ranges between 13% (arid) to 91% (Mediterranean setting). Finally, simulations with coupled precipitation and vegetation cover variations demonstrate variations in catchment erosion of 13% (arid) to 97% (Mediterranean setting). Taken together, we find that precipitation variations more strongly influence seasonal variations in erosion rates. However, the effects of seasonal variations in vegetation cover on erosion are also significant (between 5-36%) and are most pronounced in semi-arid to Mediterranean settings and least prevalent in arid and humid-temperature settings.

Keywords: Landlab, vegetation, Chilean Coastal Cordillera, biogeomorphology, seasonality, precipitation, EarthShape.

1 Introduction

Catchment erosion rates vary spatially and temporally (e.g., Wang et al., 2021) and depend on topography (e.g., slope, Carretier et al., 2018), vegetation cover and type (e.g., Zhang et al., 2011; Starke et al., 2020; Schaller and Ehlers, 2022) and precipitation rates (e.g., Cerdà, 1998; Tucker and Bras, 2000). Over annual timescales, temporal variations in catchment erosion occur in response to seasonal variations in precipitation and vegetation cover. For example, previous work has found that a significant fraction of annual erosion occurs during wet seasons, with high runoff rates (Hancock and Lowry, 2021; Leyland et al., 2016; Gao et al., 2021; Wulf et al., 2010). However, this increase in precipitation during wet seasons also promotes vegetation growth, which in turn influences erosion rates (Langbein and Schumm, 1958; Zheng, 2006; Schmid et al., 2018). Seasonal and longer-term changes in both precipitation and vegetation cover play a crucial role in intra-annual changes in erosion rates (Istanbulluoglu and Bras, 2006; Yetemen et al., 2015; Schmid et al., 2018; Sharma et al., 2021). The intensity, frequency, and seasonality of precipitation and vegetation cover change within a year depend upon the climate and ecological conditions of

38 the area of interest (Herrmann and Mohr, 2011). One means of investigating the effects of seasonality in precipitation and (or)
39 vegetation cover on erosion rates is through landscape evolution modeling (LEM), which can be parameterized for variations
40 in vegetation-dependent hillslope and fluvial processes over seasonal time scales.

41 Previous modeling and observational studies have investigated the effects of seasonality in precipitation and vegetation on
42 catchment erosion. Bookhagen et al., (2005), Wulf et al., (2010), and Deal et al., (2017) investigated the effects of stochastic
43 variations in precipitation on erosion and sediment transport in the Himalayas. They found that high variability in rainstorm
44 days (>80% of MAP) during the wet season (summer monsoon) caused high variability in the suspended sediment load. Similar
45 seasonality in sediment loads was reported in a field study in Iran, using sediment traps and erosion pins. These authors
46 concluded that wet seasons experienced maximum erosion rates (>70% of annual), which decreased in dry seasons (<10% of
47 annual) (Mosaffaie et al., 2015). Field observations in the heavily vegetated Columbian Andes concluded that soil erosion and
48 nutrient losses are significantly influenced by precipitation seasonality (Suescún et al., 2017). In contrast, work by Steegen et
49 al., (2000) in a loamy agricultural catchment in central Belgium found suspended sediment concentrations in streams were
50 lower during summer (wet) rather than winter (dry) months due to the development in vegetation cover in the wet season.
51 Other workers have found a dependence of seasonal erosion on ecosystem type. For example, Istanbuluoglu et al., (2006)
52 found a reduction in the sensitivity of soil loss potential to storm frequency in humid ecosystems compared to arid and semi-
53 arid regions. Work by Wei et al., (2015) in the semi-arid setting of the Chinese Loess Plateau, reported that significant changes
54 in vegetation related land use/land cover may contribute to long-term soil loss dynamics. However, seasonal variations in
55 runoff and sediment yield are mainly influenced by intra-annual rainfall variations. Finally, previous work in a Mediterranean
56 environment by Gabarrón-Galeote et al., (2013), described rainfall intensity as the main factor in determining hydrological
57 erosive response, regardless of the rainfall depth of an event.

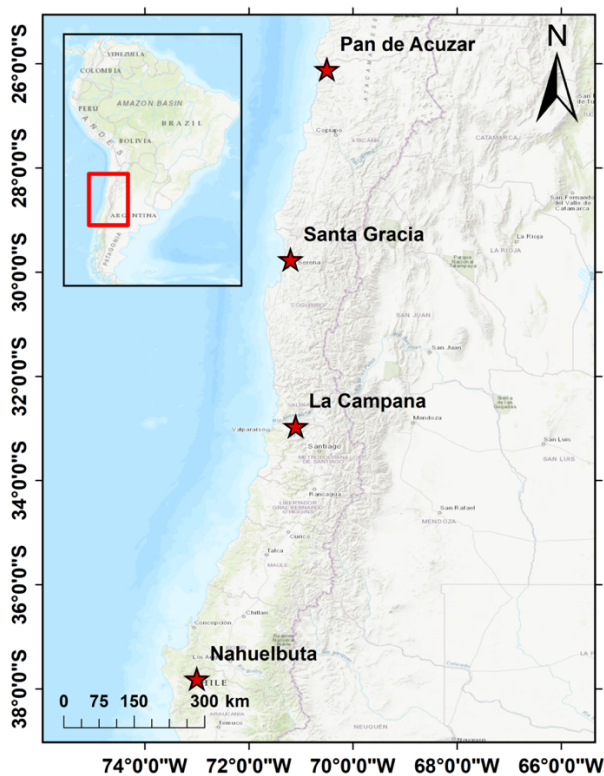
58 When looking at seasonal vegetation changes in more detail, several different studies suggest these changes are important for
59 catchment erosion. For example, Garatuza-Payán et al., (2005) emphasized that seasonal patterns in erosion are strongly
60 influenced by plant phenology as demonstrated by the changes in vegetation cover (measured by NDVI). A similar study on
61 the Loess Plateau, China, by Zheng (2006) documented decreasing soil erosion as vegetation cover increases during the wet
62 season. Work conducted in a forested setting (Zhang et al., 2014) documented the importance of tree cover as an effective
63 filter for decreasing the effects of rainfall intensity on soil structure, runoff, and sediment yield. Numerical modeling studies
64 have also found a significant impact of vegetation on erosion. For example, Zhang et al., (2019) found that when precipitation
65 was kept constant, the increase in vegetation cover resulted in a significant reduction in sediment yields (20-30% of the total
66 flux). Also, during early to mid-wet season, the species richness and evenness of plant cover both play an essential role in
67 reducing erosion rates during low rainfall events (Hou et al., 2020). However, in the case of high-intensity rainfall events at
68 the start of a wet season, when vegetation cover is low, the duration and intensity of rainfall were found to significantly affect
69 erosion rates (Hancock and Lowry, 2015). Other work conducted in a Mediterranean environment points to the coincidence of
70 peak rainfall erosivity in low vegetation cover settings, leading to an increased risk of soil erosion (Ferreira and Panagopoulos,
71 2014). Despite potentially conflicting results in the previous studies, what is clear is that seasonality in precipitation and
72 vegetation cover conspire to influence catchment erosion, although which factor (precipitation or vegetation) plays the
73 dominant role is unclear.

74 This study complements the previous work by applying a Landscape Evolution Model (LEM) to investigate seasonal transience
75 in catchment erosion due to variations in precipitation and vegetation. We do this for four locations spanning the extreme
76 climate and ecological gradient (i.e., arid, semi-arid, Mediterranean, and humid temperate) in the Chilean Coastal Cordillera.
77 Our efforts are focused on testing two hypotheses: (1) precipitation is the first-order driver of seasonal erosion rates, and (2)
78 catchment erosion in arid and semi-arid regions is more sensitive to seasonality in precipitation and vegetation than the
79 Mediterranean and humid temperate regions. To test the above hypotheses, we conduct a sensitivity analysis of fluvial and

80 hillslope erosion over four Chilean study areas to investigate the individual effects of seasonal changes in vegetation cover
81 and precipitation compared to simulations with coupled variations in precipitation and vegetation cover. We do this using a
82 two-dimensional LEM (the Landlab-SPACE software), which explicitly handles bedrock and sediment entrainment and
83 deposition. We build upon the approach of Sharma et al., (2021) with the additional consideration of soil-water infiltration.
84 Our model setup broadly representative of the present-day conditions in the Chilean Coastal Cordillera (Fig. 1) and uses
85 present-day inputs such as topography from SRTM DEMs (90 m) for four regions with different climate/ecological settings.
86 Simulations in these different ecosystems are driven by observed variations in vegetation cover from MODIS NDVI (between
87 2000 – 2019) and observed precipitation rates over the same time period from neighboring weather stations. We note that the
88 aim of this study is not to reproduce reality in these study areas. This is due to the uncertainties in the LEM initial conditions
89 and material properties, and rock uplift rates. Rather, our focus is a series of sensitivity analyses that are loosely ‘tuned’ to
90 natural conditions and observed vegetation and precipitation changes along an ecological gradient. As shown below, these
91 simplifications facilitate identifying the relative contributions of vegetation and precipitation changes on catchment erosion.

92 2 Study Areas

93 This section summarizes the geologic, climate, and vegetation settings of the four selected catchments (Fig. 1) investigated in
94 the Chilean Coastal Cordillera. These catchments (from north to south) are located in the Pan de Azúcar National Park (arid,
95 ~26°S), Santa Gracia Nature Reserve (semi-arid, ~30°S), and the La Campana (Mediterranean, ~33°S) and Nahuelbuta
96 (temperate-humid, ~38°S) national parks. Together, these study areas span ~1,300 km distance of the Coastal Cordillera. These
97 study areas are chosen for their steep climate and ecological gradient from north (arid environment with small to no shrubs) to
98 south (humid temperate environment with evergreen mixed forests) (Schaller et al., 2020). The study areas are part of the
99 German-Chilean priority research program EarthShape (www.earthshape.net) and ongoing research efforts within these
100 catchments.



101
102 **Figure 1. Study areas in the Coastal Chilean Cordillera ranging from an arid environment in the north (Pan de Azúcar),**
103 **semi-arid (Santa Gracia), Mediterranean (La Campana), and humid temperate environment in the south (Nahuelbuta).**

104 The above map is obtained from the Environmental System Research Institute (ESRI) map server
105 (https://services.arcgisonline.com/ArcGIS/rest/services/World_Topo_Map/MapServer, last access: 25 April 2022).

106 The bedrock of the four study areas is composed of granitoid rocks, including granites, granodiorites, and tonalites in Pan de
107 Azúcar, La Campana, and Nahuelbuta, respectively, and gabbro and diorites in Santa Gracia (Oeser et al., 2018). The soil
108 types in each catchment were identified as a sandy loam in three northern catchments (with high bulk density: 1300 – 1500 kg
109 m⁻³) and sandy clay loam in Nahuelbuta (with lower bulk density: 800 kg m⁻³) (Bernhard et al., 2018). The western margin of
110 Chile along the latitudes of the different study areas is characterized by a similar tectonic setting whereby an oceanic plate
111 (currently the Nazca Plate) has been subducting under the South American Plate since the Palaeozoic. Despite this common
112 tectonic setting along, slight differences in modern rock uplift rates are documented in the regions surrounding the three
113 northern catchments (i.e., < 0.1 mm yr⁻¹ for ~26 °S to ~33 °S) (Melnick, 2016) and the southern catchment (i.e., 0.04 to > 0.2
114 mm yr⁻¹ for ~38 °S over the last 4±1.2 Ma) (Glodny et al., 2008; Melnick et al., 2009). Over geologic (millennial) timescales,
115 measured denudation rates in the region range between ~0.005 to ~0.6 mm yr⁻¹ (Schaller et al., 2018). As this study focuses
116 on the sensitivity of topography to seasonal variations in vegetation and precipitation change, the tectonic parameters (rock
117 uplift) specific to each study areas are held constant. Given this, we assume a uniform rock uplift rate of 0.05 mm yr⁻¹ for
118 results presented here. This rate is broadly consistent with the range of previously reported values.

119 The climate gradient in the study areas ranges from an arid climate in Pan de Azúcar (north) with mean annual precipitation
120 (MAP) of ~11 mm yr⁻¹ to semi-arid in Santa Gracia (MAP: ~ 88 mm yr⁻¹), a Mediterranean climate in La Campana (MAP:
121 ~350 mm yr⁻¹), and a temperate-humid climate in Nahuelbuta (south) with a MAP of 1400 mm yr⁻¹ (Ziese et al., 2020). The
122 observed mean annual temperatures (MAT) also vary with latitude ranging from ~20°C in the north to ~5°C in the south
123 (Übernicker et al., 2020). The previous gradients in MAP and MAT and latitudinal variations in solar radiation result in a
124 southward increase in vegetation density (Bernhard et al., 2018). The vegetation gradient is evident from mean MODIS
125 Normalized Difference Vegetation Index (NDVI) values range from ~0.1 in Pan de Azúcar (north) to ~0.8 in Nahuelbuta
126 (south) (Didan, Kamel, 2015). In this study, NDVI values are used as a proxy for vegetation cover density, similar to the
127 approach of Schmid et al. (2018). However, one of the major limitations of using NDVI is that the values are saturated when
128 the ground is covered by shrubs or larger broad-leaved forests in regions with high biomass (Van Der Meer et al., 2001) (e.g.,
129 the catchment in humid-temperate setting). This may have implications on the shear stress partitioning ratio used to estimate
130 the sediment and bedrock erodibilities (see eq. 10-13), as the NDVI values for shrub covered land and a mature forest could
131 be similar in such cases (Huang et al., 2021).

132 This gradient in climate and vegetation cover from north to south in the Chilean Coastal Cordillera provides an opportunity to
133 study the effects of seasonal variations in vegetation cover and precipitation on catchment-scale erosion rates in different
134 climate settings.

135 3 Methods

136 3.1 Data used for model inputs

137 This study focuses on predicting and comparing the average responses in catchment erosion that occur over seasonal timescales
138 with variable precipitation and vegetation cover. However, erosion in arid and semi-arid regions can vary on sub-seasonal time
139 scales due to high-intensity storms occurring over timescales of a couple of hours or days. Hence, the model does not capture
140 the role of extreme precipitation events. Also, our preliminary modeling results suggest that the relationship between vegetation
141 cover and erosion rates may be affected by inherited simulated slope values from the previous season, which may lead to the
142 blended signal in the output.

143 Initial topography for the four selected catchments was obtained by cropping the SRTM digital elevation model (DEM) in
 144 rectangular shapes encapsulating the catchment of interest (Fig. 1). These catchments are the same as those investigated with
 145 previous soil, denudation, and geophysical studies within the EarthShape project (e.g., Bernhard et al., 2018; Oeser et al., 2018;
 146 Schaller et al., 2018; Dal Bo et al., 2019). The DEM has a spatial resolution of 90 m and is the same as the cell size used in
 147 the model (dx and dy) (SRTM data set of Earth Resources Observation And Science (EROS) Center, 2017). The present-day
 148 total relief in the catchments are ~1852 m in La Campana (~33 °S), followed by ~1063 m in Santa Gracia (~30 °S), ~809 m in
 149 Nahuelbuta (~38 °S) and ~623 m Pan de Azúcar (~26 °S). Investigated catchment sizes considered here vary between ~64 km²
 150 in Pan de Azúcar, ~142.5 km² in Santa Gracia, ~106.8 km² in La Campana, and ~68.7 km² in Nahuelbuta. We note that present-
 151 day topography as the initial condition in simulations can introduce an initial transience in erosion rates due to assumed model
 152 erosional parameters (e.g., erodibility, hillslope diffusivity) differing from actual parameters within the catchment. We address
 153 this issue through a detrending of model results described later (see Section 3.6). Furthermore, the inherent timescales at which
 154 the topography and surface processes respond (depicted by LEMs) are dependent on the physical properties incorporated and
 155 the model forcings (such as rock uplift), all of which have uncertainties associated with them. Hence, it is unlikely that the
 156 SRTM DEM used for the initial condition, is in equilibrium. Given this, the detrending of our time series of results to remove
 157 long-term transience aids in identifying seasonal transients in precipitation and vegetation cover.
 158 Precipitation data used over each study area (Fig. 3b) was acquired from the Global Precipitation Climatology Centre (GPCC)
 159 for the period 01/03/2000 to 31/12/2019 (DD/MM/YEAR). The data has a spatial resolution of 1° and a 1-day temporal
 160 resolution and comprises daily land-surface precipitation from rain gauges built on the Global Telecommunication System-
 161 based and historic data (Ziese et al., 2020). The previous data was augmented with daily precipitation weather station data
 162 from 01/02/2020 to 28/02/2020 obtained from Übernickel et al., (2020). We do this to include all the seasons between 2000 to
 163 2019, i.e., from the austral autumn of 2000 to the austral summer of 2019. The periods (months of a year) of specific seasons
 164 in the Chilean Coastal Cordillera are given in Table 1. Seasonal precipitation rates were calculated by summing daily
 165 precipitation rates at three-month intervals. The seasonality and intensity of precipitation in the wet season (winter) increases
 166 from the arid (Pan de Azúcar) to humid temperate (Nahuelbuta) region.

167 **Table 1. Months of a year corresponding to specific seasons in the Chilean Coastal Cordillera**

Seasons	Months
Summer ^{d*}	December - February
Autumn ^{w*}	March - May
Winter ^{w*}	June - August
Spring ^{d*}	September - November

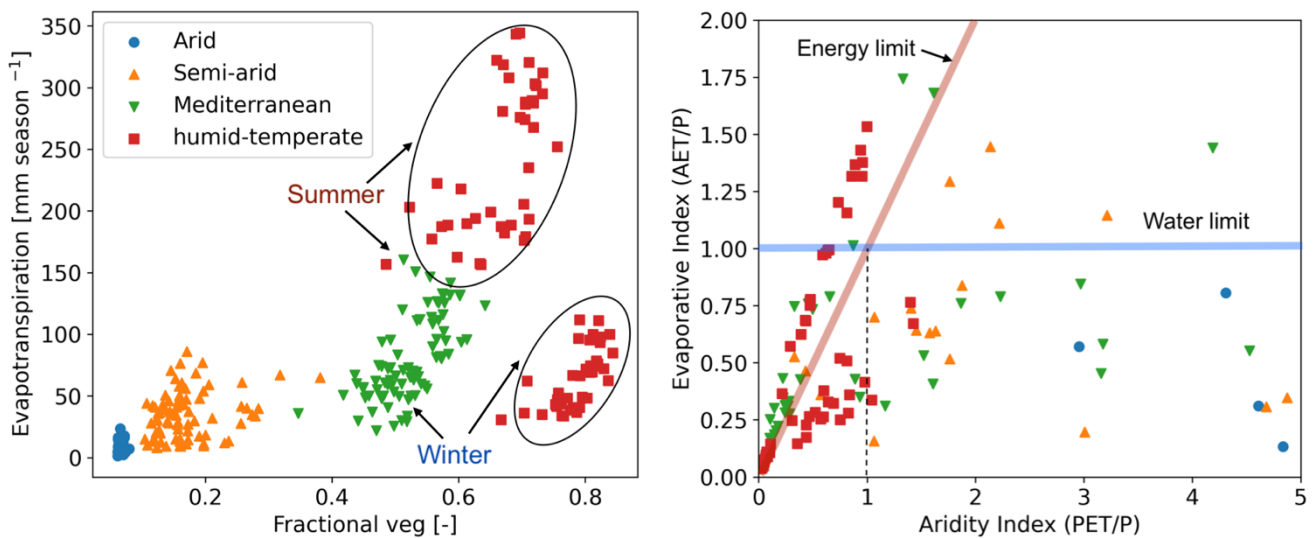
168 *d: dry season, w: wet season
 169

170 NDVI derived from remote sensing imagery has been proven as an effective tool to estimate seasonal changes in vegetation
 171 cover density (Garatuza-Payán et al., 2005). Normalized difference vegetation index (NDVI) values were obtained from
 172 MODIS (Didan, Kamel, 2015) satellite data and were used as a proxy for changes in vegetation cover in the catchments.
 173 However, the major limitation of the conversion of NDVI to vegetation cover includes a saturation problem in NDVI values
 174 that occurs in high biomass regions such as our humid-temperate setting (Huete et al., 2002). This saturation can occur if the
 175 ground is covered by shrubs, at which point the information on different plant communities for associated erosion-relevant
 176 properties is lost (e.g., rooting depth, etc.). The effect of a saturation in NDVI values could lead to uncertainties in calculating
 177 the shear stress partitioning ratio (see eq. 10-11), consequently affecting estimates of erodibility (see eq. 12-13). This is
 178 potentially important for humid-temperate climate setting characterized by high NDVI values (i.e. >0.8). The NDVI data were
 179 acquired for 20 years (01/03/2000 – 28/02/2020), with a spatial resolution of 250 m and temporal resolution of 16 days. For

180 application within the model simulations, the vegetation cover dataset was resampled using the nearest neighbour method to
 181 match the spatial resolution (90 m) of SRTM DEM and temporal resolution of 3 months. To summarize, season variations in
 182 precipitation rate and vegetation cover were applied to the simulations between 01/03/2000 and 28/02/2020 and encompass a
 183 20-year record of observation variations in these factors.

184 Additional aspects of the catchment hydrologic cycle were determined using the following approaches for the same time period
 185 previously mentioned. First, evapotranspiration (ET) data was obtained from Global Land Data Assimilation System (GLDAS)
 186 Noah version 2.1, with a monthly temporal resolution and spatial resolution of 0.25° (~ 28 km) (Beaudoin et al., 2020; Rodell
 187 et al., 2004). The data was obtained from March-2000 to February-2020. Due to the coarse resolution of the dataset, ET is
 188 assumed to be uniform over the entire catchment area. No higher resolution datasets were available over the 20-year time-
 189 period of interest.

190 Soil properties such as the grain size distribution (sand, silt, and clay fraction) and bulk density were adapted from Bernhard
 191 et al., (2018) to estimate soil water infiltration capacity in each study area. Based on these soil properties, the soils have been
 192 classified as a sandy loam (in Pan de Azúcar, Santa Gracia, and La Campana) and sandy clay loam (Nahuelbuta). Average
 193 bulk density values of 1300 kg m^{-3} , 1500 kg m^{-3} , 1300 kg m^{-3} , and 800 kg m^{-3} were used for Pan de Azúcar, Santa Gracia, La
 194 Campana, and Nahuelbuta, respectively (Bernhard et al., (2018).



195
 196 **Figure 2. Parameter correlation for observations used as model input data (i.e., seasonal precipitation, vegetation cover**
 197 **and evapotranspiration) including: (a) fractional vegetation cover (derived from NDVI) and evapotranspiration**
 198 **(derived from GLDAS NOAH), (b) Budyko curve representing the relationship between precipitation (P), potential**
 199 **evapotranspiration (PET) and actual transpiration (AET). The points above the water limit (blue line) indicate the**
 200 **contribution of soil moisture to ET. The seasons (points) above the energy limit (red line) indicate the precipitation loss**
 201 **by infiltration. The plots represent observations corresponding to Autumn of 2000 to Summer of 2019. Each data point**
 202 **represents one season and are color coded by climate of the study areas. See section 3.1 for a description of the data**
 203 **sets used.**

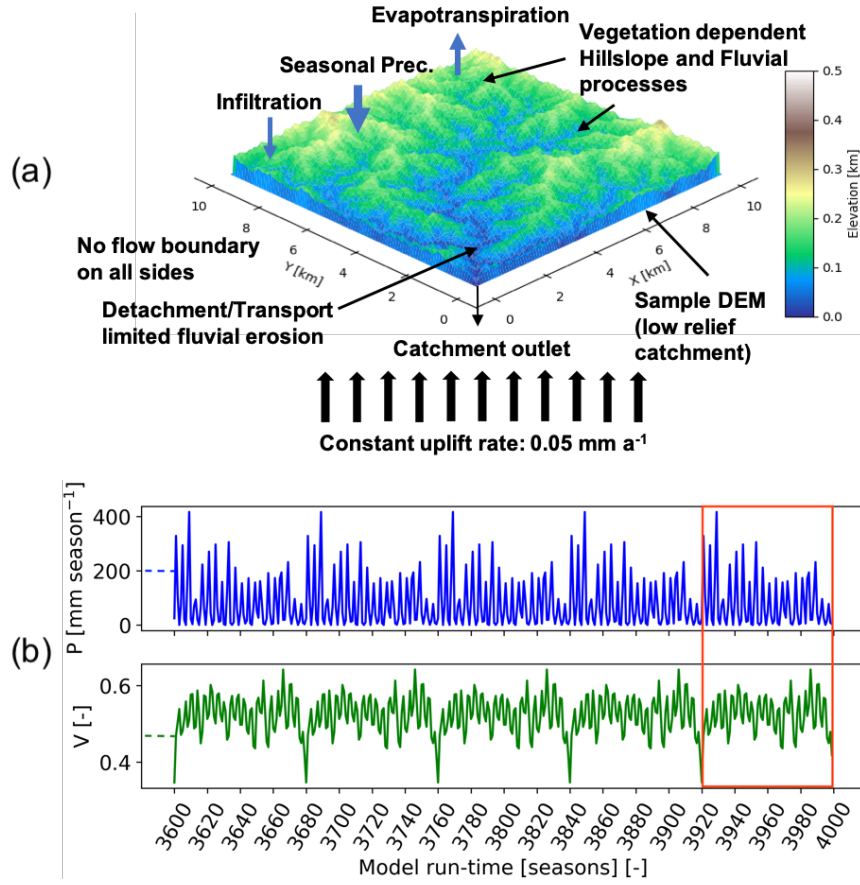
204 Figure 2 shows correlations between the model input data, such as variable climatic or hydrologic cycle metrics (i.e.,
 205 precipitation and evapotranspiration) and vegetation cover for the climate zone of each study area investigated, with other
 206 variables such as topography, soil texture etc. The relationships shown for each study area in different climate-ecological zones
 207 are based on the 20 years of data used (i.e., Autumn of 2000 – Summer of 2019). The relationship between fractional vegetation
 208 cover (V) and evapotranspiration (ET) indicates a slightly positive trend in the semi-arid setting (Fig. 2a). Whereas, the
 209 relationship in the Mediterranean setting is a steep positive gradient, with low vegetation cover (0.4– 0.55) and

210 evapotranspiration (i.e., 50 – 100 mm season⁻¹) in the winter, which increases in summer (90 – 160 mm season⁻¹) in response
211 to vegetation growth (i.e., $V = 0.55 - 0.65$). Similar trends in V and ET is indicated in the humid temperate setting during the
212 summer with V in the range of 0.55 – 0.75 and ET ranging between 150 – 350 mm season⁻¹. However, during winters, even
213 after high V in humid setting, lower values in ET are reported, with a positive trend. To help understand the datasets of
214 precipitation (P) with ET , a Budyko curve is presented in figure 2b, where the actual ET (AET) and potential ET (PET) are
215 normalized by P . In figure 2b most the data points from the humid temperate setting are above the energy limit and indicate
216 high soil water infiltration during summer seasons. Also, data points above the water limit (blue line in Fig. 2b) indicate a
217 carry-over in soil moisture from a wet season to few dry seasons in the humid, Mediterranean and semi-arid settings.

218 **3.2 Model setup**

219 We applied the Landlab landscape evolution model, a python-based modeling toolkit (Hobley et al., 2017), combined with the
220 SPACE 1.0 model (Shobe et al., 2017). The SPACE model allows coupled detachment-transport limited fluvial processes with
221 simultaneous bedrock erosion and sediment entrainment/deposition. The Landlab-SPACE programs were applied using a set
222 of runtime scripts and input files (Sharma and Ehlers, 2023) to account for vegetation and climate change effects on catchment
223 erosion (i.e., fluvial erosion and hillslope diffusion), using the approach described in Schmid et al. (2018) and Sharma et al.
224 (2021). In addition, the geomorphic processes considered involve infiltration of surface water into soil (Rengers et al., 2016)
225 based on the Green-Ampt method (Green and Ampt, 1911), and runoff modeling. The constitutive equations for the processes
226 involved in the model simulations are presented in section 3.3.

227 The model parameters (Table. A1 in Appendix) are selected for the distinct climate and ecological settings in the Chilean
228 Coastal Cordillera based on the observations presented by Schaller et al., (2018), Bernhard et al. (2018), and Übernickel et al.
229 (2020). The model state parameters (i.e., erodibility, diffusivity, rock uplift rate, etc.) in the simulations are adapted from
230 Sharma et al., (2021). The parameters pertaining to the effect of vegetation cover on erosion rates (e.g., Manning's number for
231 bare soil and reference vegetation cover, etc.) are adapted from Schmid et al. (2018). The model was simulated at a seasonal
232 scale (time step of three months) from the autumn of 2000 (01/03/2000) to the summer of 2019 (28/02/2020). Simulations
233 were conducted for a total time of 1000 years with a time-step of 1 season (3 months) with 20 years (2000 – 2019) of
234 observations in vegetation and precipitation. These 20-years of observations were repeated (looped) 50 times, to identify, and
235 detrend, long-term transient trends in catchment erosion rates due to potential differences in actual and assumed erosional
236 parameters such as the hillslope diffusivity or fluvial erodibility. The combined effects of temporally variable (at seasonal
237 scale) precipitation and vegetation cover (also spatially variable) on catchment-scale erosion rates are therefore the primary
238 factors influencing predicted erosion rates.



239

240

241

242

243

244

245

Figure 3. Schematic of the model geometry and seasonal precipitation and vegetation forcings used in this study. (a) Model setup representing sample DEM (low relief catchment) with no flow boundaries on all sides and a single catchment outlet. The model involves vegetation-dependent seasonal hillslope and fluvial processes and rainfall-infiltration-runoff modeling. (b) Seasonal precipitation and vegetation cover dataset (Mediterranean, La Campana, setting) for the last five iterations of model simulations. The results of highlighted iterations (after detrending for long-term transients) are analyzed in consecutive sections.

246

3.3 Implementation of vegetation dependent hillslope and Fluvial processes in Landlab components

247

248

249

This section includes the description of vegetation dependent hillslope and fluvial erosion routines defined in the Landlab components used in this study. Our approach is based on previous work by Istanbuluoglu (2005), Schmid et al., (2018), and Sharma et al., (2021).

250

3.3.1 Vegetation dependent hillslope processes

251

The rate of change in topography due to hillslope diffusion (Fernandes and Dietrich, 1997) is defined as follows:

252

$$\frac{\partial z}{\partial t}(\text{hillslope}) = \nabla q_s, \quad (1)$$

253

254

where q_s is sediment flux along the slope S at a time step (where, dt is 1 season) in a grid cell. We applied slope and depth-dependent linear diffusion rule following the approach of Johnstone and Hilley (2014) such that:

255

$$q_s = K_d S d_* (1 - e^{-H/d_*}), \quad (2)$$

256

257

258

where K_d is diffusion coefficient [$\text{m}^2 \text{season}^{-1}$], d_* is sediment transport decay depth [m], and H denotes sediment thickness in a grid cell at a particular time-step. In the model, the diffusion coefficient is dependent on vegetation cover present on hillslopes, which is estimated following the approach of Istanbuluoglu (2005), as follows:

259 $K_d = K_b e^{-(\alpha V)}$, (3)

260 where K_b is the diffusivity for bare soil [$\text{m}^2 \text{ season}^{-1}$] and α represents exponential decay coefficient (see Table A1 in
261 Appendix). The vegetation cover fraction in a grid cell is denoted by V .

262 3.3.2 Vegetation dependent fluvial processes

263 The fluvial erosion is estimated for a two-layer topography (i.e., bedrock and sediment are treated explicitly) in the coupled
264 detachment- / transport-limited model, SPACE 1.0 (Shobe et al., 2017). Bedrock erosion and sediment entrainment are
265 calculated simultaneously in the model in each grid cell. The total fluvial erosion is defined as:

266 $\frac{\partial z}{\partial t} (\text{fluvial}) = \frac{\partial R}{\partial t} + \frac{\partial H}{\partial t}$, (4)

267 where, the left-hand side denotes the total fluvial erosion rate. The first and second terms on the right-hand side denote the
268 bedrock erosion rate and sediment entrainment rate.

269 The rate of change of height of bedrock R per unit time [m season^{-1}] is defined as:

270 $\frac{\partial R}{\partial t} = U - E_r$, (5)

271 where E_r [m season^{-1}], is the volumetric erosion flux of bedrock per unit bed area. The previous equation implies that the
272 topography adjusts to the rock uplift rates. As result, if model prescribed erosional parameters differ from those of the modern
273 (actual) topography used for the initial condition, then a transience would occur until an equilibrium is reached between the
274 prescribed parameters and the rock uplift rate. In practice, we found these the effect of this induced transience to be small, but
275 we mitigated the effect through a linear detrending (see Section 3.6).

276 The sediment thickness is updated in each grid cell at a time-step such that the change in sediment thickness H [m] is defined
277 as a fraction of net deposition rate and solid fraction sediments, which is expressed as:

278 $\frac{\partial H}{\partial t} = \frac{D_s - E_s}{1 - \phi}$, (6)

279 where, D_s [m season^{-1}] is the deposition flux of sediment, E_s [m season^{-1}] is volumetric sediment entrainment flux per unit bed
280 area, and ϕ is the sediment porosity. The porosity in each study area are calculated from the bulk density estimations of
281 Bernhard et al. (2018), which ranges from 0.43 in the semi-arid to 0.7 in the humid-temperate settings (see Table A1).

282 Following the approach of Shobe et al. (2017), E_s and E_r are expressed as follows:

283 $E_s = (K_s q^m S^n - \omega_{cs}) \left(1 - e^{-\frac{H}{H_*}}\right)$, (7)

284 $E_r = (K_r q^m S^n - \omega_{cr}) e^{-H/H_*}$, (8)

285 where, K_s [m^{-1}] and K_r [m^{-1}] are the sediment erodibility and bedrock erodibility parameters, respectively. The threshold stream
286 power for sediment entrainment and bedrock erosion are denoted as ω_{cs} [m season^{-1}] and ω_{cr} [m season^{-1}] in above equations.
287 Bedrock roughness is denoted as H_* [m] and the term e^{-H/H_*} corresponds to the soil production from bedrock. With higher
288 bedrock roughness magnitudes, more sediment would be produced.

289 K_s and K_r were modified in each time step in the model simulations by introducing the effect of Manning's roughness to
290 quantify the effect of vegetation cover on bed shear stress in each model grid cell:

291 $\tau_v = \rho_w g (n_s + n_v)^{6/10} q^m S^n F_t$, (9)

292 where, ρ_w [kg m^{-3}] and g [m s^{-2}] are the density of water and acceleration due to gravity respectively. Manning's numbers for
 293 bare soil and vegetated surface are denoted as n_s and n_v . F_t represents shear stress partitioning ratio. Manning's number for
 294 vegetation cover and F_t are calculated as follows:

$$295 \quad n_v = n_{vr} \left(\frac{V}{V_r} \right)^w, \quad (10)$$

$$296 \quad F_t = \left(\frac{n_s}{n_s + n_v} \right)^{\frac{3}{2}}, \quad (11)$$

297 where, n_{vr} is Manning's number for the reference vegetation. Here, V_r is reference vegetation cover (*i.e.* $V = 100\%$), V is local
 298 vegetation cover in a model grid cell, and w is the empirical scaling factor.

299 By combining the stream power equation (Tucker et al., 1999; Howard, 1994; Whipple and Tucker, 1999) and above concept
 300 of the effect of vegetation on shear stress, we define modified sediment and bedrock erodibility parameters, following the
 301 approach of Schmid et al. (2018) and Sharma et al. (2021), which are as follows:

$$302 \quad K_{vs} = K_s \rho_w g (n_s + n_v)^{6/10} F_t, \quad (12)$$

$$303 \quad K_{vr} = K_r \rho_w g (n_s + n_v)^{6/10} F_t, \quad (13)$$

304 where, K_{vs} [m^{-1}] and K_{vr} [m^{-1}] are modified sediment and bedrock erodibilities respectively. These are influenced by fraction
 305 of vegetation cover V in each grid cell at time-step. Hence, K_s and K_r in Eq. (7) and Eq. (8) are replaced by K_{vs} and K_{vr} in the
 306 model, to account for vegetation-dependent fluvial erosion. The trends of K_d , K_{vs} and K_{vr} are illustrated in Fig. 3 in Sharma et
 307 al., (2021).

308 3.3.3 Vegetation dependent soil-water infiltration

309 The soil-water infiltration rate is estimated by applying the Green-Ampt equation (Green and Ampt, 1911; Julien et al., 1995),
 310 which is as follows:

$$311 \quad f(t) = K_e \left(1 + \frac{\Psi \Delta \theta}{F} \right), \quad (14)$$

312 where $f(t)$ is the infiltration rate [m s^{-1}] at time t , K_e is the effective hydraulic conductivity [m s^{-1}], F is the cumulative infiltration
 313 [m], Ψ is the suction at the wetting front [m], and $\Delta \theta$ is the difference between saturated and initial volumetric moisture content
 314 [$\text{m}^3 \text{m}^{-3}$]. Effective hydraulic conductivity is highly variable and anisotropic; hence, it was considered to be uniform with a
 315 value of $1 \times 10^{-6} \text{ m s}^{-1}$ for each catchment.

316 Following the approach of Istanbuluoglu and Bras, (2006) for loamy soils, the soil-water infiltration was modified to account
 317 for variable vegetation cover in each grid cell, as follows:

$$318 \quad I_c(t) = f(t)(1 - V(t)) + 4f(t)(V(t)), \quad (15)$$

$$319 \quad I_a(t) = \text{Min}[P(t), I_c(t)], \quad (16)$$

320 where I_c is the infiltration capacity and V is the vegetation cover (between 0 and 1) in a model grid cell at time-step t . Values
 321 used in the simulations for the parameters in equations 14-16 are provided in appendix Table A1.

322 3.3.4 Estimation of runoff rates

323 The precipitation rates [m season^{-1}] are subjected to soil-water infiltration [m season^{-1}] and evapotranspiration [m season^{-1}] to
 324 estimate the seasonal runoff rates [mm season^{-1}]. The runoff rates (R) at every time step (t) are calculated using the actual soil-
 325 water infiltration (I_a) and the actual evapotranspiration (ET) as follows,

326 $R(t) = P(t) - I_a(t) - ET(t)$, (17)

327 where, P is the precipitation amount in a season. This relationship was applied in the model grid cells with non-zero sediment
328 thickness, which is updated at each time-step (see eq. 6) in order to facilitate infiltration. If the sediment is not present in the
329 grid cell, there is no soil-water infiltration. As ET is the input parameter, there may be instances of higher ET than P in the
330 summer seasons in the humid, Mediterranean and semi-arid settings. This is evident in figure 2b where the minimum of both
331 values is used as ET in the given time-step.

332 **3.4 Boundary and initial conditions**

333 The boundaries are closed (no flow) on all sides, with a single stream outlet at the point of minimum elevation at a boundary
334 node (Fig. 3). In contrast to previous modeling studies (Schmid et al., 2018; Sharma et al., 2021) in the same study areas, we
335 used present-day topography as the initial condition in each study area for simulations instead of a synthetic topography
336 produced during a model spin-up phase in Landlab. This implies four different initial conditions for four study areas, such as
337 topography, climate, vegetation, sediment thickness and porosity etc. Initial sediment cover thickness is considered uniform
338 across the model domain, and was approximated based on observations presented in Schaller et al., (2018) and Dal Bo et al.,
339 (2019). The sediment thicknesses used are 0.2 m in the arid (AZ), 0.45 m in semi-arid (SG), 0.6 m in the Mediterranean (LC),
340 and 0.7 m in humid temperate (NA) catchments. The rock uplift rate is kept constant throughout the entire model run as 0.05
341 mm yr⁻¹, adapted from a similar study (Sharma et al., 2021). However, in a 1000-year simulation, differences in base level
342 (rock uplift) effects have limited impact on the variations in results interpreted here.

343 **3.5 Overview of simulations conducted**

344 The simulations were designed to identify the sensitivity of erosion rates to seasonal variations in either precipitation rates or
345 vegetation cover, as well as the more realistic scenario of coupled seasonal variations in both vegetation cover and
346 precipitation. We evaluated this sensitivity with the following three scenarios:

- 347 1. Scenario 1: Influence of constant (mean seasonal) precipitation with seasonal variations in vegetation cover
348 catchment-scale erosion rates.
- 349 2. Scenario 2: Influence of seasonal variation in precipitation and constant (mean seasonal) vegetation cover on
350 catchment-scale erosion rates.
- 351 3. Scenario 3: Influence of coupled seasonal variations in both precipitation and vegetation cover on catchment-scale
352 erosion rates.

353 The results for scenarios 1 – 3 are illustrated in sections 4.1, 4.2, and 4.3, respectively.

354 **3.6 Detrending of results for long term transients**

355 Model simulations were conducted for 1,000 years using 20 years [March-2000 – Feb-2020] of observations in vegetation
356 cover, and precipitation and were repeated 50 times for a total simulation duration of 1000 years. Simulations presented here
357 were conducted on the present-day topography, which was updated at each time-step in the LEM (based on rock uplift rates
358 and erosion) to allow for the application of observed time series of precipitation and vegetation change in different ecosystems
359 and study areas. This choice of setting comes with the compromise that the erosional parameters (e.g., diffusivity, erodibility,
360 etc.) used in the model (see Table A1 in Appendix) are likely not the same as those that led to the present-day catchment
361 topography. As a result, a long-term transient in erosion rates is expected as the model tries to reach an equilibrium with
362 assumed erosional parameters. To correct for any long-term transients in erosion influencing our interpretations, we conducted
363 a linear detrending of the results to remove any long-term variations. The detrending was conducted through a linear regression

364 over entire time series of 1000 years and the values were corrected using the slope of the regression line. Hence, the detrended
365 model results for the last 20 years were analyzed and discussed in sections 4 and 5. In practice, the detrending of time series
366 did not impart a significant change to the results presented.

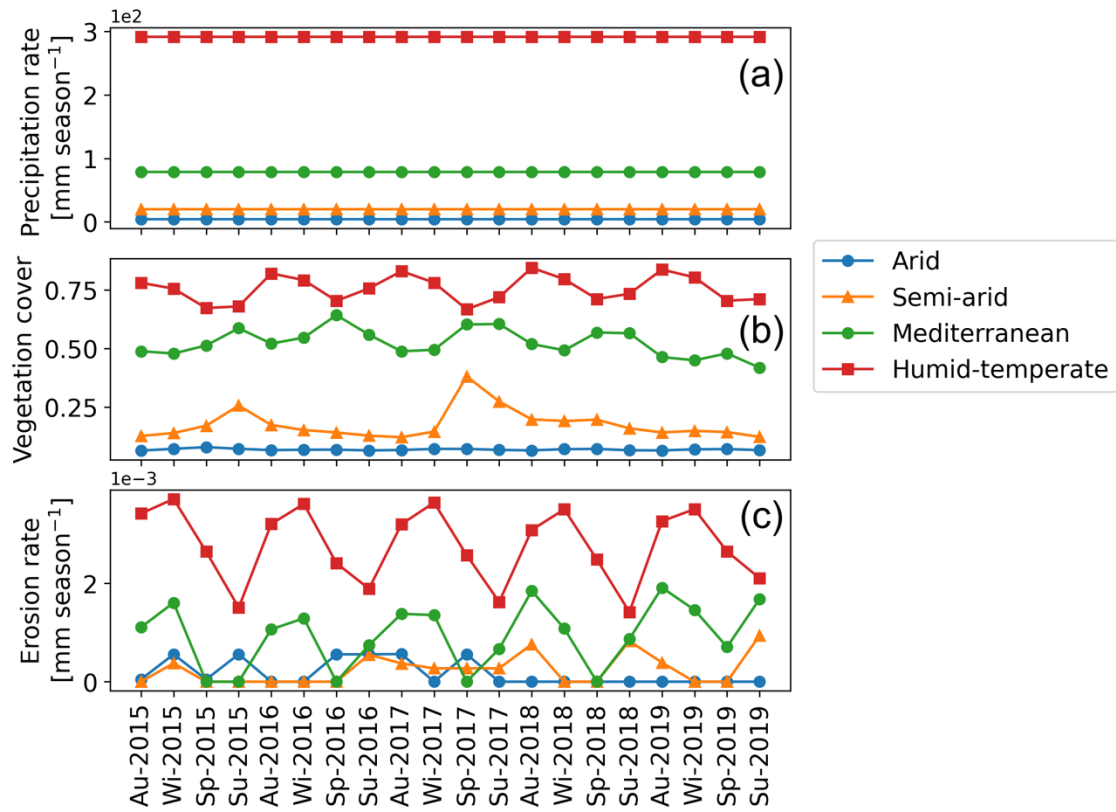
367 **4 Results**

368 In the following sections, we focus our analysis on the mean catchment erosion rates over seasonal (3 months) time scales (see
369 Table. 1). In all scenarios, the rock uplift rate was kept constant at 0.05 mm yr^{-1} following the approach of Sharma et al. (2021).
370 For simple representation, the results of the last five years of the last cycle of transient simulations starting from Autumn-2015
371 to Summer-2019 are displayed in Fig. 4, 6, and 8 (after detrending, see section 3.6). The results for the entire time series
372 (Autumn-2000 – Summer-2019) are available in the supplement (Fig. 1 – 3). The precipitation and erosion rates are shown
373 with the units $[\text{mm season}^{-1}]$.

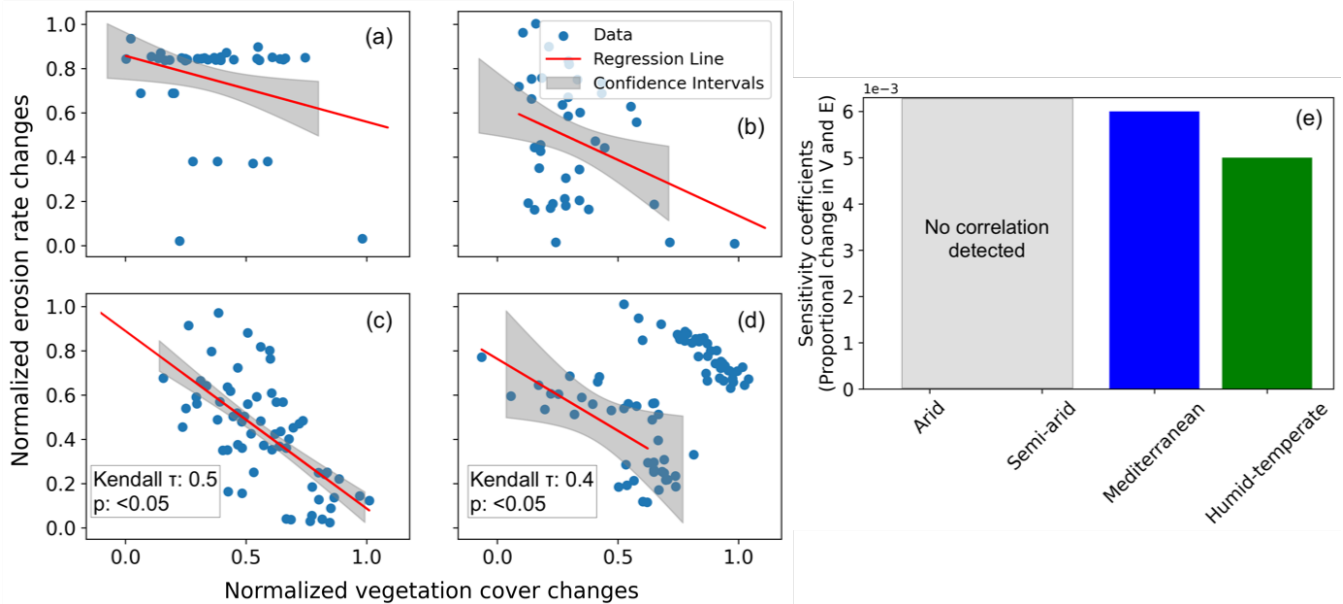
374 **4.1 Scenario 1: Influence of constant precipitation and seasonal variations in vegetation cover on erosion rates**

375 In scenario 1, vegetation cover (MODIS NDVI from March 2000 to February 2020) fluctuates seasonally (Fig. 4b), and
376 precipitation rates are kept constant at the seasonal mean (i.e., MAP divided by the number of seasons in a year) during the
377 entire time-series (Fig. 4a) (Ziese et al., 2020). The range of seasonal vegetation cover variations (and mean seasonal
378 precipitation rates) are observed as $0.06 - 0.08$ ($3.92 \text{ mm season}^{-1}$), $0.1 - 0.4$ ($20.16 \text{ mm season}^{-1}$), $0.35 - 0.65$ ($79 \text{ mm season}^{-1}$),
379 and $0.5 - 0.85$ ($292 \text{ mm season}^{-1}$) for the arid, semi-arid, Mediterranean and, humid temperate settings, respectively (Figs.
380 4a-b). The predicted mean catchment seasonal erosion rates range between $0 - 6 \times 10^{-4} \text{ mm season}^{-1}$, $0 - 9.4 \times 10^{-4} \text{ mm}$
381 season^{-1} , $0 - 2.3 \times 10^{-3} \text{ mm season}^{-1}$, and $1.2 \times 10^{-3} - 4 \times 10^{-3} \text{ mm season}^{-1}$ for the arid, semi-arid, Mediterranean and
382 humid temperate settings, respectively (Fig. 4c).

383 To analyze the relationships between the relative changes in forcings and responses, seasonal changes in vegetation cover and
384 erosion rates were normalized between 0 and 1 and plotted in Figs. 5a-d. An inverse relationship and negative correlation
385 (Kendall-tau correlation coefficient: $0.4 - 0.5$) is visible between the normalized catchment erosion rates and vegetation cover
386 for the dry season and wet season separately in the humid temperate (Fig. 5d) and Mediterranean settings (Fig. 5c). The
387 observed inversely linear relationship between vegetation and erosion changes in Mediterranean and humid-temperate settings
388 demonstrates the prevalence of fluvial (water-driven) and overland flow processes within these catchments, with hillslope
389 diffusion playing a negligible role. In contrast, no correlation was found for the arid and semi-arid settings.



390
 391 **Figure 4. Results of simulations with constant seasonal precipitation and variable vegetation over last 5 years (Autumn-**
 392 **2015 – Summer-2019)** of last cycle of transient-state model run representing: (a) mean catchment seasonal precipitation
 393 rates [mm season⁻¹], (b) mean catchment seasonal vegetation cover [-], and (c) mean catchment seasonal erosion rates
 394 [mm season⁻¹].



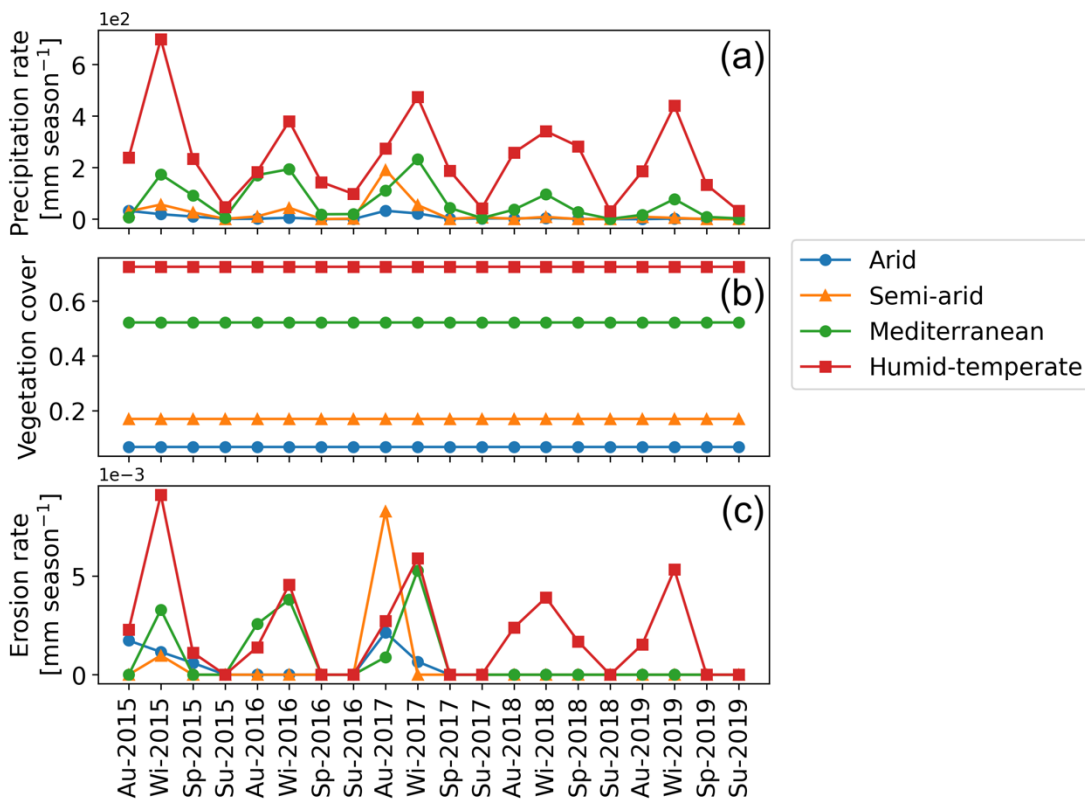
395
 396 **Figure 5. Seasonal changes (normalized) in vegetation cover and erosion rates for the scenario with constant**
 397 **precipitation and seasonal changes in vegetation cover in (a) arid, (b) semi-arid, (c) Mediterranean, and (d) humid-**
 398 **temperate settings, with the information on confidence interval (grey shading) and Kendall-tau correlation coefficients.**
 399 **(e) Sensitivity coefficients for proportional changes in vegetation cover and erosion rates based on the slope and**
 400 **intercept of the regression lines for the above environmental settings. The sensitivity coefficient is defined as the slope**
 401 **of the regression line presented in sub-sections a-d.**

402 The sensitivity coefficients based on slope and intercept of the regression lines (Figs. 5a-d) are plotted in Fig. 5e. The results
 403 indicate a higher sensitivity of erosion rates to seasonal vegetation changes in the Mediterranean setting relative to humid-
 404 temperate setting. However, in the arid and semi-arid settings, the lack of a significant correlation in the change in vegetation
 405 cover and erosion rates leads to a low sensitivity. This is owed to very low mean precipitation rates ($<20 \text{ mm season}^{-1}$) in the
 406 arid and semi-arid settings. The predicted erosion rates are relatively low (e.g., $<0.004 \text{ mm season}^{-1}$) in this scenario, due to
 407 low mean precipitation rates, which are primarily subjected to infiltration and evapotranspiration in these drier settings.

408 4.2 Scenario 2: Influence of seasonal variations in precipitation and constant vegetation cover on erosion rates

409 In scenario 2, vegetation cover (MODIS NDVI from Mar-2000 – Feb-2020) is kept constant at the mean seasonal vegetation
 410 cover (Fig. 6b) and precipitation rates vary seasonally (Mar-2000 – Feb-2020) (Fig. 6a). The range of seasonal precipitation
 411 rate variations are observed in the range of $0 - 32.42 \text{ mm season}^{-1}$, $0 - 191.66 \text{ mm season}^{-1}$, $0.03 - 417 \text{ mm season}^{-1}$, and $26 -$
 412 $987 \text{ mm season}^{-1}$ in the arid, semi-arid, Mediterranean and, humid temperate settings, respectively.

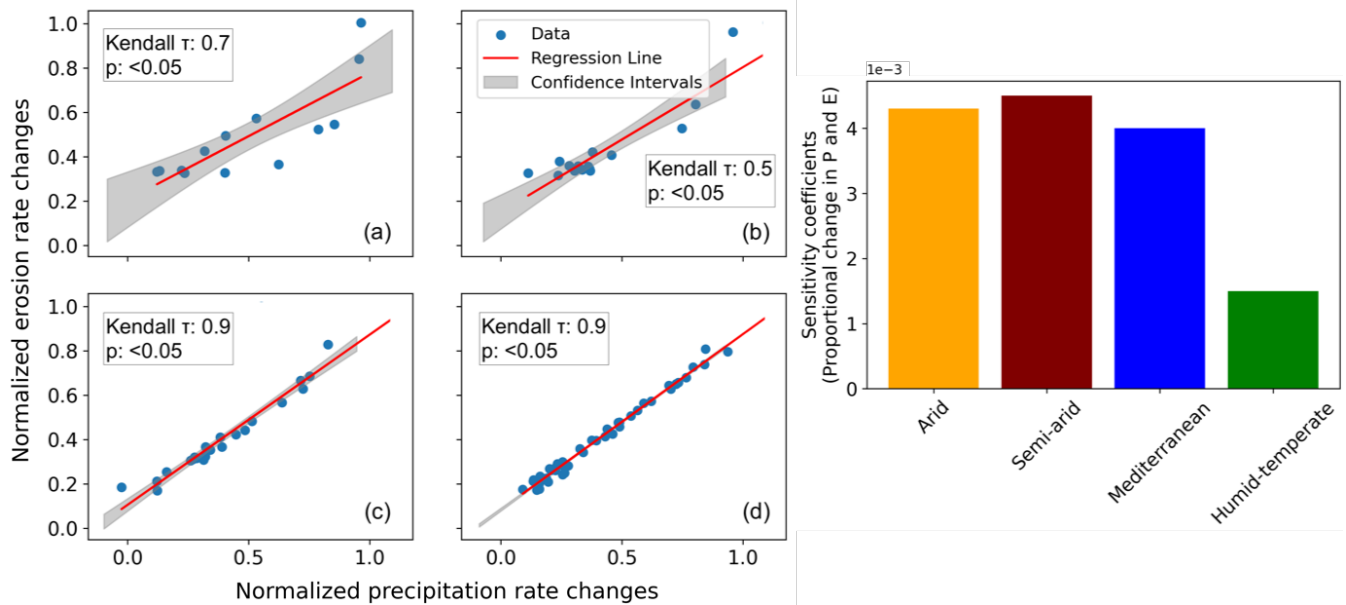
413 The simulated mean catchment seasonal erosion rates are observed in the range of $0 - 2 \times 10^{-3} \text{ mm season}^{-1}$, $0 - 8.3 \times 10^{-3}$
 414 mm season^{-1} , $0 - 1.37 \times 10^{-2} \text{ mm season}^{-1}$, and $0 - 1.3 \times 10^{-2} \text{ mm season}^{-1}$ in the arid, semi-arid, Mediterranean and, humid
 415 temperate settings, respectively (Fig. 6c).



416
 417 **Figure 6. Results of simulations with variable seasonal precipitation and constant vegetation over the last 5 years**
 418 **(Autumn-2015 – Summer-2019) of last cycle of transient-state model run representing: (a) mean catchment seasonal**
 419 **precipitation rates [mm season^{-1}], (b) mean catchment seasonal vegetation cover [-], and (c) mean catchment seasonal**
 420 **erosion rates [mm season^{-1}].**

421 Similar to scenario 1, the changes in seasonal precipitation and erosion rates were normalized between 0 and 1 and plotted in
 422 Figs. 7a-d. A strong positive correlation (Kendall-tau correlation coefficient ranging from 0.5 in semi-arid to 0.9 in
 423 Mediterranean and humid-temperate settings) in the normalized precipitation and erosion rates changes is predicted with the
 424 majority of the data points within the 95% confidence interval in all the settings. The sensitivity coefficients based on the
 425 proportional changes in precipitation and erosion rates, indicate the highest sensitivity in semi-arid settings) with $\sim 5\%$, $\sim 11\%$

426 and ~67% lower sensitivities in the arid, Mediterranean, and humid-temperate settings, respectively (Fig. 7e). This may be
 427 owed to the occasional El Niño events with extremely high precipitation occurring in the arid and semi-arid settings (with
 428 sparse vegetation cover) in our study areas.



429
 430 **Figure 7. Seasonal changes (normalized) in precipitation and erosion rates for the scenario with seasonal changes in**
 431 **precipitation rates and constant vegetation cover in (a) arid, (b) semi-arid, (c) Mediterranean, and (d) humid-temperate**
 432 **settings, with the information on confidence interval (grey shading) and Kendall-tau correlation coefficients. (e)**
 433 **Sensitivity coefficients for proportional changes in precipitation and erosion rates based on the slope and intercept of**
 434 **the regression lines for the above environmental settings. The sensitivity coefficient is defined as the slope of the**
 435 **regression line presented in sub-sections a-d.**

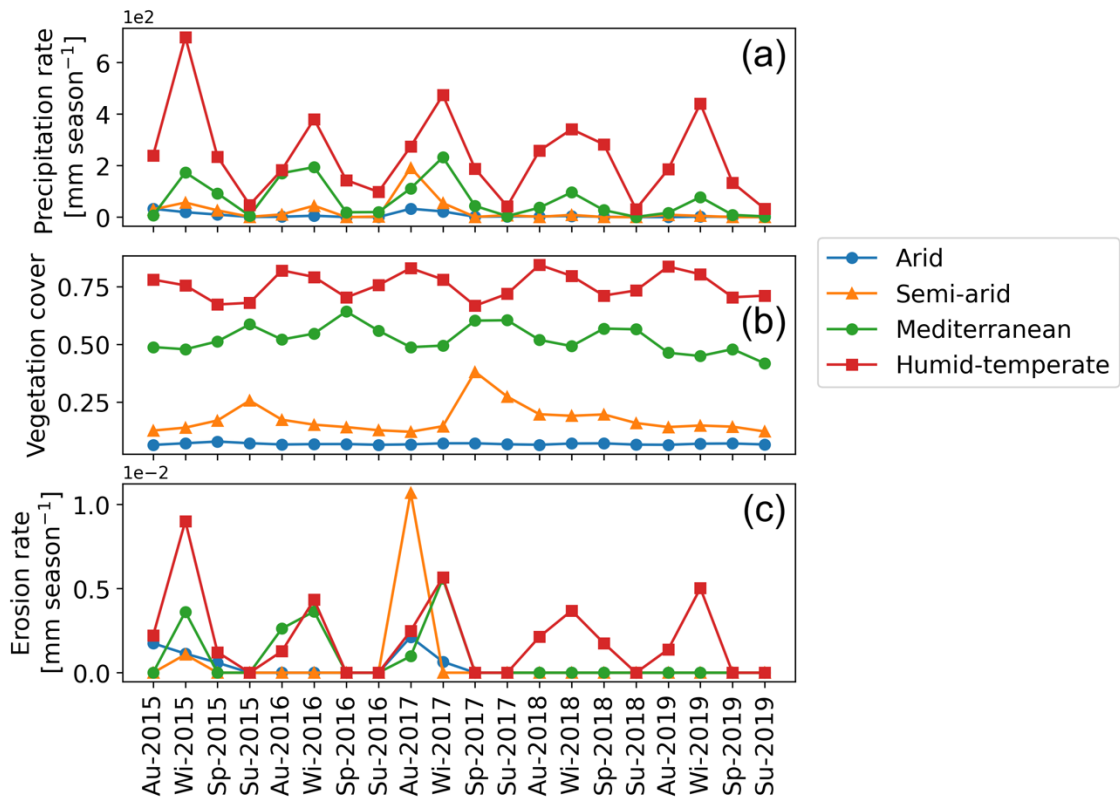
436 **4.3 Scenario 3: Influence of coupled seasonal variations in both precipitation and vegetation cover on erosion rates**

437 In this scenario, coupled variations in seasonal vegetation cover (MODIS NDVI from Mar-2000 – Feb-2020) (Fig. 8b) and
 438 precipitation rates are presented for the years 2000 - 2019 (Fig. 8a). The range of seasonal precipitation rates (and seasonal
 439 vegetation cover, V) variations are 0 – 32.42 mm season⁻¹ (V= 0.06 – 0.08), 0 – 191.66 mm season⁻¹ (0.1 – 0.38), 0.03 – 417
 440 mm season⁻¹ (0.35 – 0.65), and 26 – 987 mm season⁻¹ (0.5 – 0.85) in the arid, semi-arid, Mediterranean and, humid temperate
 441 settings, respectively (Figs. 8a-b). The mean catchment seasonal erosion rates range between 0 – 2×10^{-3} mm season⁻¹, 0 –
 442 1×10^{-2} mm season⁻¹, 0 – 1.4×10^{-2} mm season⁻¹, and 0 – 1.4×10^{-2} mm season⁻¹ in the arid, semi-arid, Mediterranean
 443 and, humid temperate settings, respectively (Fig. 8c).

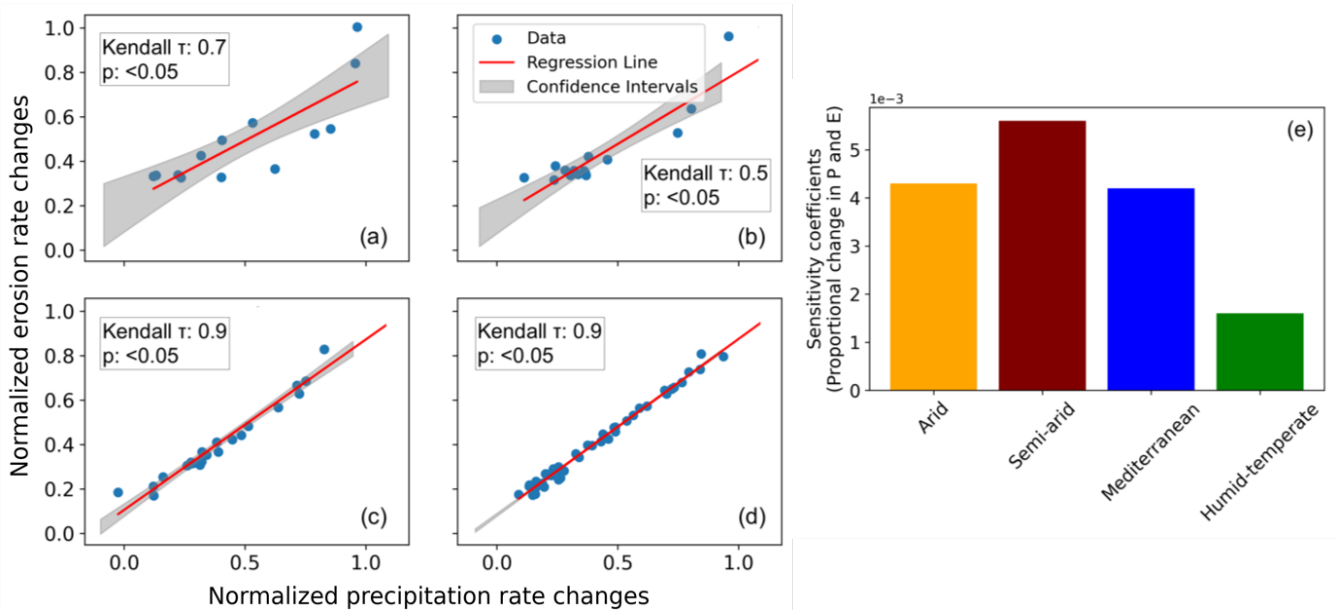
444 Changes in precipitation on erosion rates were normalized between 0 and 1 and plotted in figures. 9a-d. Similar to the results
 445 from scenario 2, a strong positive correlation was predicted in all the environmental settings. The sensitivity coefficients based
 446 on the proportional changes in precipitation and erosion rates, indicate the highest sensitivity in the semi-arid settings with
 447 ~25% and ~71% lower sensitivities in arid and Mediterranean, and humid-temperate settings, respectively (Fig. 9e). Similarly,
 448 the isolated effect of changes the in the vegetation cover on erosion rates (Fig. 10) does not yield a significant correlation in
 449 arid, semi-arid and Mediterranean settings. However, we observe a strong negative correlation in the humid-temperate setting
 450 (Fig. 10d) during the wet season (Kendall tau correlation coefficient: -0.6, with >95% significance level). Hence, the sensitivity
 451 coefficients in this case are not plotted.

452 The similarity in results obtained from scenarios 2 and 3 suggest a first-order control of seasonal precipitation changes on
 453 erosion rates (~70% higher sensitivity to changes in precipitation), with less significance to vegetation cover changes. For

454 example, the sensitivity of erosion to precipitation rate changes in semi-arid setting is predicted as ~70% higher to that of
 455 humid-temperate setting in both the scenarios.
 456



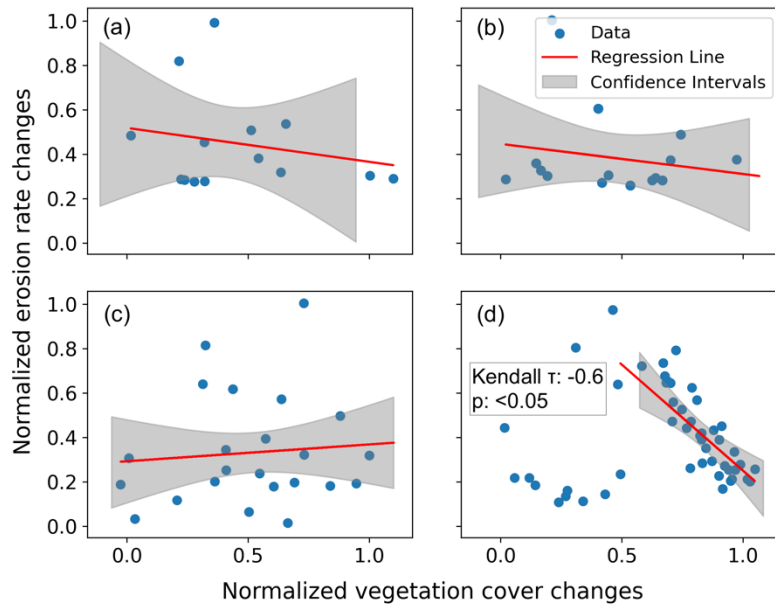
457
 458 **Figure 8. Results of simulations with coupled variations in seasonal precipitation and vegetation over the last five years**
 459 **(Autumn-2015 – Summer-2019) of the last cycle of transient-state model run representing: (a) mean catchment seasonal**
 460 **precipitation rates [mm season⁻¹], (b) mean catchment seasonal vegetation cover [-], and (c) mean catchment seasonal**
 461 **erosion rates [mm season⁻¹].**



462
 463 **Figure 9. Seasonal changes (normalized) in precipitation and erosion rates for the scenario with coupled seasonal**
 464 **changes in both precipitation rates and vegetation cover in (a) arid, (b) semi-arid, (c) Mediterranean, and (d) humid-**
 465 **temperate settings, with the information on confidence interval (grey shading) and Kendall-tau correlation coefficients.**

466 (e) Sensitivity coefficients for proportional changes in precipitation and erosion rates based on the slope and intercept
 467 of the regression lines for the above environmental settings. The sensitivity coefficient is defined as the slope of the
 468 regression line presented in sub-sections a-d.

469



470

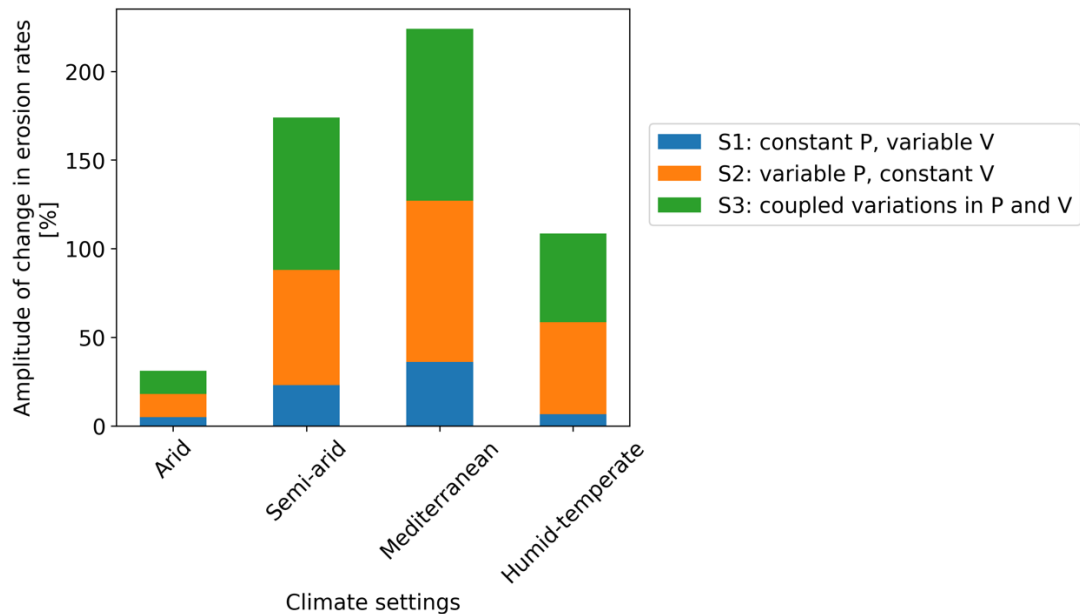
471 **Figure 10. Seasonal changes (normalized) in vegetation cover and erosion rates for the scenario with coupled seasonal**
 472 **changes in both precipitation rates and vegetation cover in (a) arid, (b) semi-arid, (c) Mediterranean, and (d) humid-**
 473 **temperate settings, with the information on confidence interval (grey shading) and Kendall-tau correlation coefficients.**

474 **5 Discussion**

475 **5.1 Synthesis of the amplitude of change in erosion rates for model scenarios 1-3**

476 The amplitude of change of mean catchment erosion rates [in percentage] varies at a seasonal scale (Fig. 11) between the study
 477 areas. The amplitude of change in erosion rates to their respective mean values was estimated (Fig. 11) using the coefficient
 478 of variation in percent (standard deviation divided by the mean of a dataset). The coefficient of variation is a statistical tool to
 479 compare multiple variables free from scale effects. It is a dimensionless quantity (Brown, 1998). This comparison represents
 480 the sensitivity of each catchment to changing seasonal weather for all three model scenarios (sections 4.1 – 4.3).

481 In scenario 1, with seasonal variations in vegetation cover and constant seasonal precipitation (Fig. 11), the amplitude of
 482 change in erosion rates ranges between 5% in the arid and 36% in Mediterranean setting. The above results support the findings
 483 of Zhang et al. (2019), which used the soil and water assessment tool (SWAT) based on NDVI and climate parameters. They
 484 observed 20-30% of the total change in sediment yield with constant precipitation and variable vegetation cover.



485

486

487

488

489

Figure 11. Stacked bar plot depicting the amplitude of change in seasonal erosion rates (relative to their respective means). Scenario 1 is shown in blue and had variable vegetation cover and constant precipitation rates. Scenario 2 is shown in orange and had constant vegetation cover and variable precipitation rates, and scenario 3 is shown in green and represents the simulation with coupled variations in vegetation cover and precipitation rates.

490

491

492

493

494

495

496

497

498

499

500

501

502

503

504

In scenario 2, with constant vegetation cover and variable precipitation rates (Fig. 11), the amplitude of change in erosion rates ranges from 13% in the arid setting (AZ) to 52%, 65%, and 91% in humid-temperate (NA), semi-arid (SG) and Mediterranean (LC) settings, respectively. A similar trend is observed in scenario 3 with coupled variations in vegetation cover and precipitation rates (Fig. 11), with the amplitude of change in erosion rates between 13% in the arid setting up to 50%, 86%, and 97% in the humid-temperate, semi-arid and Mediterranean settings, respectively. The magnitude of erosion rate changes is amplified in scenario 3, especially in the semi-arid setting (e.g., ~21% increase in the amplitude of change from scenario 2 to scenario 3). This amplification could be owed to the 35% change in vegetation cover in the semi-arid setting (Fig. 8). Overall, these observations indicate a high sensitivity of erosion in semi-arid and Mediterranean environments compared to arid and humid-temperate settings.

505

506

507

508

509

510

511

The pattern of erosion rate changes in scenarios 1-3 implies a dominant control of precipitation variations (rather than vegetation cover change) on catchment erosion rates at a seasonal scale. This interpretation is consistent with previous observational studies. For example, a field study by Suescún et al. (2017) in the Columbian Andes highlighted the significant influence of precipitation seasonality (over vegetation cover seasonality) on runoff and erosion rates. An observational catchment-scale study in the semi-arid Chinese Loess Plateau by Wei et al. (2015) indicated that intra-annual precipitation variations were a significant contributor to monthly runoff and sediment yield variations.

5.2 Synthesis of catchment erosion rates over wet and dry seasons

506

507

508

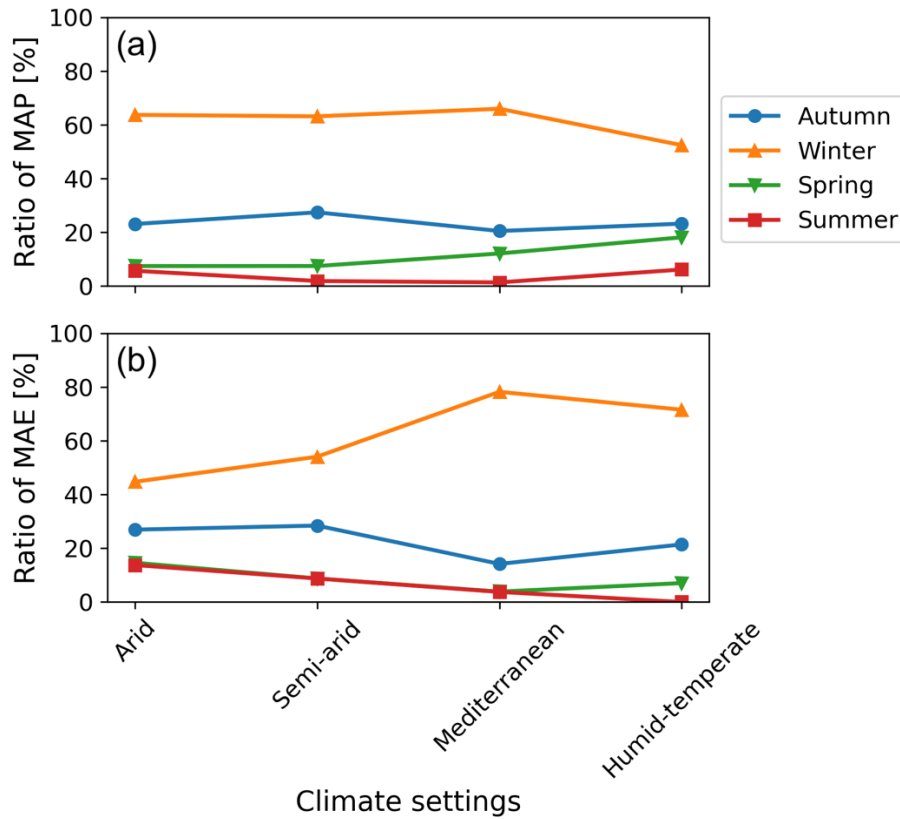
509

510

511

In this section, we discuss the ratio of seasonal precipitation and erosion rates with the mean annual precipitation (MAP) (Fig. 12a) and mean annual erosion (MAE) (Fig. 12b) during different seasons (i.e., autumn – summer) in a year, averaged over the last cycle of the transient simulations (i.e., depicting the erosion rate predictions for 2000 – 2019). These are defined as the ratio of the mean erosion (and precipitation) rates in a season (e.g., winter) to the mean annual erosion rates (and MAP) during the last 20 years of the transient simulations. This was done to identify the impact of precipitation during wet seasons (in this case, winter) in influencing the annual erosion rates. This analysis was performed for the simulation results of scenario 3 for

512 different climate and ecological settings (i.e., arid to humid-temperate). We do this specifically with scenario 3 results to
 513 capture the trends in erosion rates with coupled variations in model input (i.e., precipitation and vegetation cover).

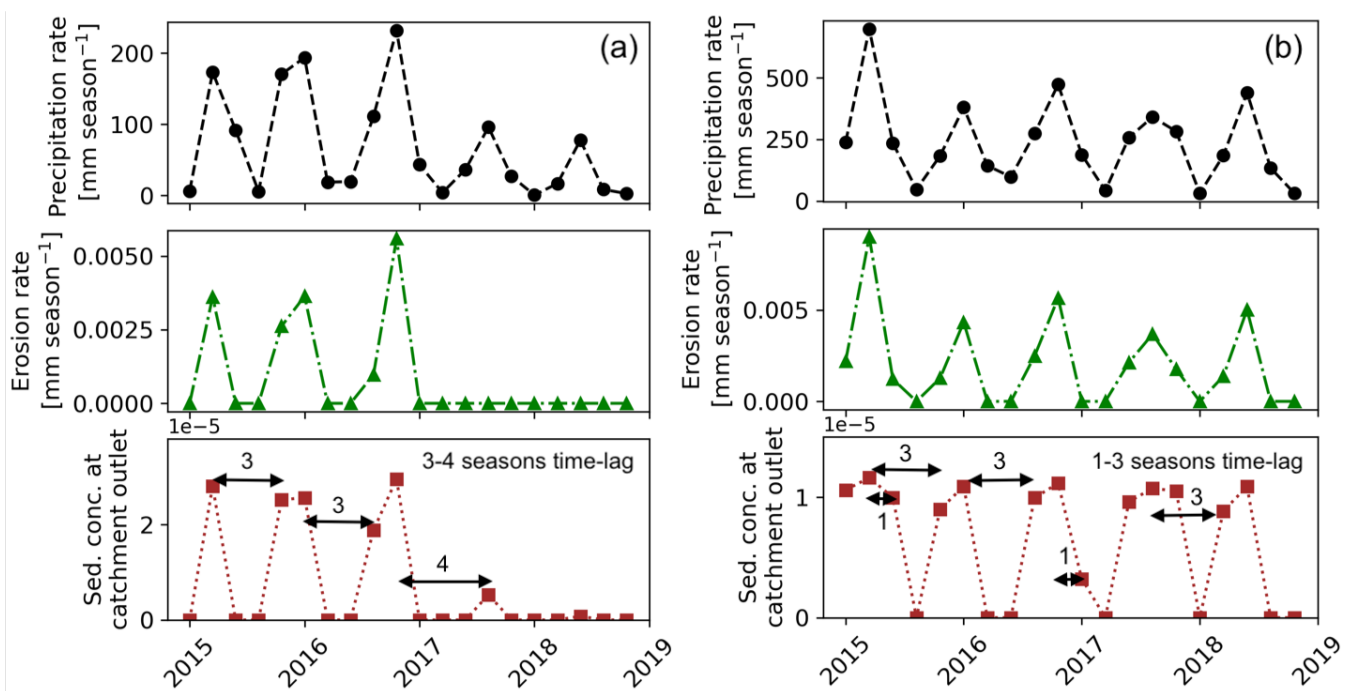


514
 515 **Figure 12. The ratio of seasonal precipitation and erosion rates to mean annual precipitation (MAP) and mean annual**
 516 **erosion (MAE) during the last cycle of transient simulations results from scenario 3 (coupled seasonal variations in**
 517 **precipitation and vegetation cover). The plots correspond to (a) the ratio of MAP per season [%] and (b) ratio of MAE**
 518 **per season [%]. Each color and point style represent the ratio for a distinct climate setting i.e., arid, semi-arid,**
 519 **Mediterranean, and humid-temperate settings.**

520 The values for the ratio of MAP during different seasons (Fig. 12a) depicts winter (June-August) and summer (December-
 521 February) as the wettest and driest seasons of the year, respectively. For example, all study areas receive >50% and <6% of
 522 MAP during winters and summers. The same is reflected in Fig. 12b with 45%, 55%, 78%, and 71% of MAE in the arid, semi-
 523 arid, Mediterranean, and humid-temperate settings, respectively, during winters. On the contrary, during summers the share of
 524 MAE decreases from 14% in the arid setting to 1% in the humid-temperate setting. The Autumn (March-May) receives lower
 525 precipitation amounts that range from 20–30% of MAP in the study areas. Arid and semi-arid settings experience a relatively
 526 higher share of MAE (e.g., ~30%) than the Mediterranean and humid temperate settings (e.g., ~15-20%). The Spring season
 527 experiences relatively higher erosion rates despite a smaller share of MAP in arid and semi-arid settings. For example, the arid
 528 and semi-arid settings experience 10-14% of the MAE for ~7% of MAP. At the same time, the Mediterranean and humid-
 529 temperate settings experience 5-7% of MAE for ~12-18% of MAP during Spring. Overall, we find that arid and semi-arid
 530 settings experience <15% and ~50% of MAE during the wet (winter) and dry (summer) seasons. The above relationship is
 531 amplified for the Mediterranean and humid-temperate settings with <5% and >70% of MAE occurring during wet and dry
 532 seasons, respectively. The latter is in agreement with an observational study by Mosaffaie et al., (2015) in a Mediterranean
 533 catchment in Iran. More specifically, Mosaffaie et al., (2015) used field observations from 2012-2013 to conclude that
 534 maximum erosion rates (>70%) are observed during the wet season, which decreases in the dry season (<10%).

535 **5.3 Consideration of transient sediment dynamics in model results**

536 This section discusses the impact of lag times from when sediment is eroded from a source area until it leaves the catchment
 537 outlet. This analysis was conducted because in natural systems, when sediment is eroded from its source, it takes time to leave
 538 the catchment (in this case the model domain) and recorded as eroded in our analysis. According to field studies and modeling
 539 experiments, this time lag is usually more than a season (i.e. 3 months) (e.g., Buendia et al., (2016)). Also, these time lags are
 540 dependent on the morphology of the catchment in addition to the geology, climate and vegetation cover of the area. Hence, the
 541 simulation results (of scenario 3 with coupled variations in seasonal precipitation and vegetation cover) for the catchments in
 542 the Mediterranean (Fig. 13a) and humid-temperate settings (Fig. 13b) are compared. We do this to capture the topological
 543 influence on lag times, as both the catchments have different topographies and surface area. The time-lags in precipitation,
 544 erosion and concentration of sediment leaving the catchment outlet are analyzed and presented in Fig. 13. The concentration
 545 of sediment is defined as a dimensionless quantity (Q_s/Q) estimated from sediment flux (Q_s) and discharge rates (Q) at
 546 catchment outlet at a particular time-step in the model simulation.



547
 548 **Figure 13. Simulation results (scenario 3: coupled variations in precipitation in vegetation cover) to capture the time-**
 549 **lags in precipitation, erosion rates and sediment concentration at catchment outlet over the last five years (Autumn-**
 550 **2015 – Summer-2019) of the last cycle of transient-state model run for the catchments in: (a) Mediterranean and (b)**
 551 **humid-temperate setting.**

552 In the Mediterranean settings, these time lags range from 3 to 4 seasons, and are relatively large (e.g., from wet season 2016
 553 to wet season of 2017, see Fig. 13a), despite high channel relief of 1800 m. This signal is also blended due to the relatively
 554 large surface area of the catchment (i.e., 106 km²). However, in humid-temperate setting, these time lags range from 1 to 3
 555 seasons (Fig. 13b) with relatively lower channel relief (i.e., 800 m) and smaller catchment area (i.e., 69 km²). Hence, the time
 556 lags in the study areas are dominated by the changes in vegetation cover and precipitation magnitude and frequency in the
 557 region with minimal influence of topology of the catchment. This is owed to the primary influence of vegetation and
 558 precipitation modulations rather than the base level changes in the catchment topology on the lag times in sediment dynamics.
 559 In the catchments in both these climate settings, the pulse of sediment leaving the catchment is fairly distributed with the
 560 maximum concentration of sediment leaving the catchment in the same wet season when it is eroded from its source. These
 561 time-lags would result in enhanced sensitivity of the proportional changes in erosion rates to the changes in seasonal

562 precipitation and (or) vegetation cover, as the sediment is transported even in the seasons when the sediment is not eroded
563 from its source (e.g., wet season in 2017 in both the above climate settings). This poses a limitation to the current study and is
564 again revisited in the model limitations (section 5.5).

565 **5.4 Comparison to previous studies**

566 In this section, we relate the broad findings of this study to the previously published observational studies. In an observational
567 study in an agrarian drainage basin in the Belgian Loam Belt, Steegen et al., (2000) evaluated sediment transport over various
568 time scales (including seasonal). They observed lower sediment fluxes during the seasons with high vegetation cover. In
569 addition, an observational study by Zheng (2006) investigated the effect of vegetation changes on soil erosion in the Loess
570 Plateau, China, and concluded that soil erosion was significantly reduced (up to ~50%) after vegetation restoration. Another
571 observational study in semi-arid grasslands in the Loess Plateau, China, by Hou et al., (2020) highlighted a considerable
572 reduction in erosion rates due to the development of richness and evenness of the plant community in the early to the mid wet
573 season. Our results from scenario 1 (seasonal variations in vegetation cover with constant precipitation rates) support the
574 findings of the above studies whereby a negative correlation (Kendal τ : -0.4 – -0.5) was found between vegetation cover and
575 erosion rates in humid-temperate and Mediterranean settings (see Fig. 5).

576 A catchment-scale observational study in Baspa Valley, NW Himalayas (Wulf et al., 2010), analyzed seasonal precipitation
577 gradients and their impact on fluvial erosion using weather station observations (1998 – 2007). The study observed a positive
578 correlation between precipitation and sediment yield variability, demonstrating the summer monsoon's first-order control on
579 erosion processes. An observational study by Wei et al., (2015) in Loess Plateau, China, evaluated erosion and sediment
580 transport under various vegetation types and precipitation variations. They found that significant changes in landscape pattern
581 and vegetation coverage (i.e., land use land cover) might contribute to long-term dynamics of soil loss. However, seasonal
582 variations in runoff and sediment yield were mainly influenced by rainfall seasonality. In comparison to the results of this
583 study, we find the similarity in the patterns of erosion rates in scenario 2 (variable precipitation and constant vegetation cover)
584 and scenario 3 (coupled variations in precipitation and vegetation) are consistent with the findings of Wei et al., (2015). For
585 example, the amplitude of change in erosion rates (Fig. 10) in scenarios 2 and 3 differ by 0%, 6%, and -2% in the arid,
586 Mediterranean, and humid-temperate settings, respectively. However, this difference is enhanced in the semi-arid region (i.e.,
587 ~23%) due to a relatively high degree of variation (~25%) in seasonal vegetation cover change.

588 Finally, an observational study in the Columbian Andes by Suescún et al., (2017) assessed the impact of seasonality on
589 vegetation cover and precipitation and found higher erosion rates in regions with steeper slopes. Another study by Chakrapani
590 (2005) emphasized the direct impact of local relief and channel slope on sediment yield in natural rivers. The broad findings
591 of the above studies agree with our results from scenarios 1-3, as we find higher erosion rates in the Mediterranean and humid-
592 temperate regions with steeper topography (mean slope ~20 deg), which encounter high seasonality (and intensity) in
593 precipitation.

594 **5.5 Model Limitations**

595 The model setup used in this study was designed to quantify the sensitivity of erosion rates in different climate and ecological
596 settings with variations in precipitation rates and vegetation cover at seasonal scales. We represent the degree of variations in
597 erosion rates in terms of changes in the amplitude (with respect to the mean) for different model scenarios (see sections 4.1 –
598 4.3).

599 Our modeling approach used several simplifying assumptions that warrant discussion and are avenues for investigation in
600 future studies. For example, model results presented here successfully capture the major surface processes, including
601 vegetation-dependent erosion and infiltration, sediment transport, and surface runoff. However, groundwater flow is not

602 considered in the current study, and how the reentry of groundwater into streams over seasonal scales would influence
603 downstream erosion. The reason is that groundwater flow modeling includes a high amount of heterogeneity and anisotropy
604 and requires much finer grid sizes (<1m) and smaller time steps (in seconds to hours). Thus, due to the large grid-cell size (90
605 m), timescales (monthly), and high uncertainty in subsurface hydrologic parameters we were unable to evaluate the effects of
606 groundwater flow on our results. Furthermore, this study assumed uniform lithologic and hydrologic parameters (e.g., vertical
607 hydraulic conductivity, initial soil moisture, evapotranspiration, erodibility, etc.) over the entire catchment. As said earlier,
608 these properties are subject to a high level of uncertainty and heterogeneity, the best fitting parameters, based on previously
609 published literature (e.g., Schaller et al., 2018; Bernhard et al., 2018; Schmid et al., 2018; Sharma et al., 2021) are used for the
610 model simulations. However, the heterogeneity in vegetation cover and related soil-water infiltration per grid cell is used in
611 this study. For the heterogeneity in vegetation cover, we use MODIS-derived NDVI as a proxy of vegetation cover. According
612 to Garatuza-Payán et al. (2005), NDVI is assumed as an effective tool for estimating seasonal changes in vegetation cover
613 density. However, the spatial resolution (250 m) of the NDVI dataset is lower than that of the SRTM DEM (90 m) used in the
614 study. Nevertheless, the difference in spatial resolution of vegetation cover and topography might introduce ambiguity in the
615 model results. Furthermore, transient dynamics associated with sediment storage in the model is not incorporated in the study
616 to capture the time lag required for the eroded sediment to move out of the model domain. As the LEM (SPACE 1.0) used in
617 this study shuffles between detachment- and transport-limited fluvial erosion, we suspect that in such short timescales (3
618 months) and in small catchments, detachment-limited fluvial erosion is dominant. Hence, any sediment removed from its
619 source is transported out of the domain in a given time-step. However, it is recommended for future studies considering larger
620 or lower gradient catchments, where sediment storage may be more significant than documented here, an analysis of erosion
621 at a local scale (e.g., at individual model grid cells) is recommended.

622 A final limitation stems from several generalized model parameters (e.g., rock uplift rate, erodibility, diffusivity, etc.) applied
623 to the SRTM DEM (as initial topography). We did this to capture the effects of seasonality in precipitation and vegetation
624 cover in modern times (2000 - 2019). However, the current topography might not have evolved with the same tectonic and
625 lithological parameters. To address this limitation, we conducted simulations for 50 iterations and detrended the model results
626 to remove those transient effects (see section 3.6). This limitation can be handled in future studies by parameterizing the model
627 to the current topography using stochastic (e.g., Bayesian) techniques (e.g., Stephenson et al., 2006; Avdeev et al., 2011). As
628 this study was aimed to capture the control of seasonal precipitation and (or) vegetation changes on the relative variability of
629 erosion rates, the above limitation may not pose a problem in the model results.

630 **6 Summary and Conclusions**

631 In this study, we applied a landscape evolution model to quantify the impact of seasonal variations in precipitation and
632 vegetation on catchment averaged erosion rates. We performed this in regions with varied climate and ecology including: arid,
633 semi-arid, Mediterranean, and humid-temperate settings. Three sets of simulations were designed to model erosion rates for
634 (a) scenario 1: constant precipitation and variable vegetation cover, (b) scenario 2: variable precipitation and constant
635 vegetation cover, and (c) scenario 3: coupled variations in precipitation and vegetation cover. The main conclusions derived
636 from this study are as follows:

- 637 1. Scenario 1, with variable vegetation cover and constant precipitation (Fig. 4), resulted in small variations in seasonal
638 erosion rates ($<0.02 \text{ mm yr}^{-1}$) in comparison to the other scenarios. The amplitude of change in seasonal erosion rates
639 (relative to the mean) is the smallest in humid-temperate setting and maximum in the Mediterranean setting (Fig.
640 10a). For example, it ranges from 5% in the arid setting (Pan de Azúcar) to 23% and 36% in the semi-arid (Santa
641 Gracia) and Mediterranean settings (La Campana), respectively.

- 642 2. Scenario 2, with constant vegetation cover and variable precipitation (Fig. 6), results in relatively higher seasonal
643 erosion rates ($<0.06 \text{ mm yr}^{-1}$) in comparison to scenario 1. The amplitude of change in seasonal erosion rates (relative
644 to the mean) is smallest in the arid setting and largest in the Mediterranean setting (Fig. 10b). For example, it ranges
645 from 13% in the arid setting (Pan de Azúcar) to 52%, 65%, and 91% in the humid-temperate (Nahuelbuta), semi-arid
646 (Santa Gracia), and Mediterranean settings (La Campana), respectively.
- 647 3. Scenario 3, with coupled variations in vegetation cover and precipitation (Fig. 8), results in similar seasonal erosion
648 rates ($<0.06 \text{ mm yr}^{-1}$) to scenario 2. Similarly, the amplitude of change in seasonal erosion rates (relative to the mean)
649 is the smallest in the arid setting and the largest in the Mediterranean setting (Fig. 10c). For example, it ranges from
650 13% in the arid setting (Pan de Azúcar) to 50%, 86%, and 97% in the humid-temperate (Nahuelbuta), semi-arid (Santa
651 Gracia), and Mediterranean settings (La Campana), respectively. A significant increase (from scenario 2) in the
652 variation in erosion rates ($\sim 21\%$) is owed to the $\sim 25\%$ variation in vegetation cover in semi-arid settings.
- 653 4. All study areas experience maximum and minimum erosion during wet and dry seasons, respectively (Fig. 11b).
654 However, the difference (in maximum and minimum) is amplified from the arid ($\sim 30\%$) to the Mediterranean and
655 humid-temperate settings ($\sim 70\text{-}75\%$). This is owed to the range of amplitude of precipitation rate change (Fig. 7)
656 increasing from the arid (e.g., $\sim 9 \text{ mm}$) to humid-temperate settings (e.g., $\sim 543 \text{ mm}$) in wet and dry seasons.

657 Finally, this study was motivated by testing the hypotheses that (1) if precipitation variations primarily influence seasonal
658 erosion, then the influence of seasonal vegetation cover changes would be less significant, and (2) catchment erosion in drier
659 settings is more sensitive to seasonality in precipitation and vegetation, than wetter settings. With respect to hypothesis 1, we
660 found that seasonal precipitation variations primarily drive catchment erosion and the effects of vegetation cover variations
661 are secondary. Results presented here (Fig. 10b) support this interpretation with a high amplitude of change in erosion rates
662 (with respect to means) ranging from 13 to 91% for the scenario with constant vegetation cover and seasonal precipitation
663 variations. However, the effect of seasonal vegetation cover changes is also significant (Fig. 10a), ranging between 5 – 36%.
664 Hence, the first hypothesis is partially confirmed, but the magnitude of response depends on the ecological zone investigated.
665 Concerning hypothesis 2, we found that seasonal changes in catchment erosion are more pronounced in the semi-arid and
666 Mediterranean settings and less pronounced in the arid and humid temperate settings. This interpretation is supported by Fig.
667 10c, with a significantly high amplitude of change in catchment erosion in semi-arid ($\sim 86\%$) and Mediterranean ($\sim 97\%$)
668 settings with relatively lower changes in humid temperate ($\sim 50\%$) and arid ($\sim 13\%$) settings, partially confirming the
669 hypothesis.

670

671

672

673

674

675

677 **Table A1. Input parameters with corresponding units for the landscape evolution model**

Model Parameters	Values
Grid spacing (dx)	90 m
Model runtime (totalT)	1000 years (2000 - 2019 repeated over 50 times)
time-step (dt)	1 season (3 months)
Rock uplift rate (U) ¹	1.25 x 10 ⁻⁵ [m season ⁻¹] (or 0.05 [mm a ⁻¹])
Initial sediment thickness (H _{initial}) ²	20 (A*), 45 (SA*), 60 (M*), 70 (HT*) [cm]
Bedrock erodibility (Kr) ¹	2 x 10 ⁻⁹ [m ⁻¹]
Sediment erodibility (Ks) ¹	2 x 10 ⁻⁸ [m ⁻¹]
Reach scale bedrock roughness (H*) ¹	1 [m]
Porosity (Φ) ⁴	0.51 (A*), 0.43 (SA*), 0.51 (M*), 0.7 (HT*) [-]
Fraction of fine sediments (Ff) ¹	0.2 [-]
Effective terminal settling velocity (Vs) ¹	2.5 [mm season ⁻¹]
m, n ¹	0.6, 1 [-]
Bedrock erosion threshold stream power (ω _{cr}) ¹	1.25 x 10 ⁻⁵ [m season ⁻¹]
Sed. entr. threshold stream power (ω _{cs}) ¹	1.25 x 10 ⁻⁶ [m season ⁻¹]
Bare soil diffusivity (K _b) ¹	2.5 x 10 ⁻⁴ [m ² season ⁻¹]
Exponential decay coefficient (α) ¹	0.3 [-]
Critical channel formation area (A _{crit}) ³	1 x 10 ⁶ [m ²]
Reference vegetation cover (V _r) ³	1 (100%)
Manning's number for bare soil (n _s) ³	0.01 [-]
Manning's number for ref. vegetation (n _v) ³	0.6 [-]
Scaling factor for vegetation influence (w) ³	1 [-]
Soil bulk density (B) ⁴	1300 (A*), 1500 (SA*), 1300 (M*), 800 (HT*) [kg m ⁻³]
Soil type ⁴	sandy loam (A*, SA*, and M*); sandy clay loam (HT*)
Initial soil moisture (s) ⁵	0.058 (A*), 0.02 (SA*), 0.053 (M*), 0.15 (HT*) [m ³ m ⁻³]

678 ¹Sharma et al. (2021), ²Schaller et al. (2018), ³Schmid et al. (2018), ⁴Bernhard et al. (2018), ⁵Übernickel et al. (2020).

679 *A: arid; SA: semi-arid; M: Mediterranean; HT: humid-temperate setting.

680 **Code and data availability**681 The code and data used in this study are freely available via Zenodo (<https://doi.org/10.5281/zenodo.8033782>, Sharma and
682 Ehlers, 2023).683 **Author contributions**684 HS and TAE designed the initial model setup and simulation programs. HS and TAE conducted model modifications,
685 simulation runs, and analysis. HS prepared the initial paper draft and both authors contributed to revisions.686 **Competing interests**

687 The authors declare that they have no conflict of interest.

688 **Acknowledgments**

689 We acknowledge the support from the Open Access Publishing fund of the University of Tübingen. We would like to thank
690 two anonymous reviewers and Omer Yetemen for their constructive reviews. We also thank Simon Mudd for editing this
691 paper.

692 **Financial support**

693 This research has been supported by the Deutsche Forschungs Gemeinschaft (grant nos. EH329/14-2, SPP-1803, and Research
694 Training Group 1829 Integrated Hydrosystem Modelling).

695 **Review Statement**

696 This paper was edited by Simon Mudd and reviewed by two anonymous reviewers and Omer Yetemen.

697 **References**

- 698 Avdeev, B., Niemi, N. A., and Clark, M. K.: Doing more with less: Bayesian estimation of erosion models with detrital
699 thermochronometric data, *Earth Planet. Sci. Lett.*, 305, 385–395, <https://doi.org/10.1016/j.epsl.2011.03.020>, 2011.
- 700 Barnhart, K. R., Glade, R. C., Shobe, C. M., and Tucker, G. E.: Terrainbento 1.0: a Python package for multi-model analysis
701 in long-term drainage basin evolution, *Geosci. Model Dev.*, 12, 1267–1297, <https://doi.org/10.5194/gmd-12-1267-2019>,
702 2019.
- 703 Beaudoin, H., Rodell, M., and NASA/GSFC/HSL: GLDAS Noah Land Surface Model L4 monthly 0.25 x 0.25 degree,
704 Version 2.1, <https://doi.org/10.5067/SXAVCZFAQLNO>, 2020.
- 705 Bernhard, N., Moskwa, L.-M., Schmidt, K., Oeser, R. A., Aburto, F., Bader, M. Y., Baumann, K., von Blanckenburg, F.,
706 Boy, J., van den Brink, L., Brucker, E., Büdel, B., Canessa, R., Dippold, M. A., Ehlers, T. A., Fuentes, J. P., Godoy, R.,
707 Jung, P., Karsten, U., Köster, M., Kuzyakov, Y., Leinweber, P., Neidhardt, H., Matus, F., Mueller, C. W., Oelmann, Y.,
708 Oses, R., Osses, P., Paulino, L., Samolov, E., Schaller, M., Schmid, M., Spielvogel, S., Spohn, M., Stock, S., Stroncik, N.,
709 Tielbörger, K., Übernickel, K., Scholten, T., Seguel, O., Wagner, D., and Kühn, P.: Pedogenic and microbial interrelations to
710 regional climate and local topography: New insights from a climate gradient (arid to humid) along the Coastal Cordillera of
711 Chile, *CATENA*, 170, 335–355, <https://doi.org/10.1016/j.catena.2018.06.018>, 2018.
- 712 Bookhagen, B., Thiede, R. C., and Strecker, M. R.: Abnormal monsoon years and their control on erosion and sediment flux
713 in the high, arid northwest Himalaya, *Earth Planet. Sci. Lett.*, 231, 131–146, <https://doi.org/10.1016/j.epsl.2004.11.014>,
714 2005.
- 715 Brown, C. E.: Coefficient of Variation, in: *Applied Multivariate Statistics in Geohydrology and Related Sciences*, Springer,
716 Berlin, Heidelberg, 1998.
- 717 Buendia, C., Vericat, D., Batalla, R. J., and Gibbins, C. N.: Temporal Dynamics of Sediment Transport and Transient In-
718 channel Storage in a Highly Erodible Catchment: LINKING SEDIMENT SOURCES, RAINFALL PATTERNS AND
719 SEDIMENT YIELD, *Land Degrad. Dev.*, 27, 1045–1063, <https://doi.org/10.1002/ldr.2348>, 2016.
- 720 Carretier, S., Tolorza, V., Regard, V., Aguilar, G., Bermúdez, M. A., Martinod, J., Guyot, J.-L., Hérail, G., and Riquelme,
721 R.: Review of erosion dynamics along the major N-S climatic gradient in Chile and perspectives, *Geomorphology*, 300, 45–
722 68, <https://doi.org/10.1016/j.geomorph.2017.10.016>, 2018.
- 723 Cerdà, A.: The influence of aspect and vegetation on seasonal changes in erosion under rainfall simulation on a clay soil in
724 Spain, *Can. J. Soil Sci.*, 78, 321–330, <https://doi.org/10.4141/S97-060>, 1998.
- 725 Chakrapani, G. J.: Factors controlling variations in river sediment loads, *Curr. Sci.*, 88, 569–575, 2005.

- 726 Deal, E., Favre, A. C., and Braun, J.: Rainfall variability in the Himalayan orogen and its relevance to erosion processes:
727 RAINFALL VARIABILITY IN THE HIMALAYAS, *Water Resour. Res.*, 53, 4004–4021,
728 <https://doi.org/10.1002/2016WR020030>, 2017.
- 729 Didan, Kamel: MOD13Q1 MODIS/Terra Vegetation Indices 16-Day L3 Global 250m SIN Grid V006,
730 <https://doi.org/10.5067/MODIS/MOD13Q1.006>, 2015.
- 731 Earth Resources Observation And Science (EROS) Center: Shuttle Radar Topography Mission (SRTM) Void Filled,
732 <https://doi.org/10.5066/F7F76B1X>, 2017.
- 733 Fernandes, N. F. and Dietrich, W. E.: Hillslope evolution by diffusive processes: The timescale for equilibrium adjustments,
734 *Water Resour. Res.*, 33, 1307–1318, <https://doi.org/10.1029/97wr00534>, 1997.
- 735 Ferreira, V. and Panagopoulos, T.: Seasonality of Soil Erosion Under Mediterranean Conditions at the Alqueva Dam
736 Watershed, *Environ. Manage.*, 54, 67–83, <https://doi.org/10.1007/s00267-014-0281-3>, 2014.
- 737 Gabarrón-Galeote, M. A., Martínez-Murillo, J. F., Quesada, M. A., and Ruiz-Sinoga, J. D.: Seasonal changes in the soil
738 hydrological and erosive response depending on aspect, vegetation type and soil water repellency in different Mediterranean
739 microenvironments, *Solid Earth*, 4, 497–509, <https://doi.org/10.5194/se-4-497-2013>, 2013.
- 740 Gao, P., Li, Z., and Yang, H.: Variable discharges control composite bank erosion in Zoige meandering rivers, *CATENA*,
741 204, 105384, <https://doi.org/10.1016/j.catena.2021.105384>, 2021.
- 742 Garatuzza-Payán, J., Sánchez-Andrés, R., Sánchez-Carrillo, S., and Navarro, J. M.: Using remote sensing to investigate
743 erosion rate variability in a semiarid watershed, due to changes in vegetation cover, *IAHS Publ*, 292, 144–151, 2005.
- 744 Glodny, J., Gräfe, K., Echtler, H., and Rosenau, M.: Mesozoic to Quaternary continental margin dynamics in South-Central
745 Chile (36–42°S): the apatite and zircon fission track perspective, *Int. J. Earth Sci.*, 97, 1271–1291,
746 <https://doi.org/10.1007/s00531-007-0203-1>, 2008.
- 747 Green, W. H. and Ampt, G. A.: Studies on Soil Physics., *J. Agric. Sci.*, 4, 1–24, <https://doi.org/10.1017/S0021859600001441>,
748 1911.
- 749 Hancock, G. and Lowry, J.: Hillslope erosion measurement—a simple approach to a complex process, *Hydrol. Process.*, 29,
750 4809–4816, 2015.
- 751 Hancock, G. and Lowry, J.: Quantifying the influence of rainfall, vegetation and animals on soil erosion and hillslope
752 connectivity in the monsoonal tropics of northern Australia, *Earth Surf. Process. Landf.*, 46, 2110–2123,
753 <https://doi.org/10.1002/esp.5147>, 2021.
- 754 Herrmann, S. M. and Mohr, K. I.: A Continental-Scale Classification of Rainfall Seasonality Regimes in Africa Based on
755 Gridded Precipitation and Land Surface Temperature Products, *J. Appl. Meteorol. Climatol.*, 50, 2504–2513,
756 <https://doi.org/10.1175/JAMC-D-11-024.1>, 2011.
- 757 Hopley, D. E. J., Adams, J. M., Nudurupati, S. S., Hutton, E. W. H., Gasparini, N. M., Istanbuluoglu, E., and Tucker, G. E.:
758 Creative computing with Landlab: an open-source toolkit for building, coupling, and exploring two-dimensional numerical
759 models of Earth-surface dynamics, *Earth Surf. Dyn.*, 5, 21–46, <https://doi.org/10.5194/esurf-5-21-2017>, 2017.
- 760 Hou, J., Zhu, H., Fu, B., Lu, Y., and Zhou, J.: Functional traits explain seasonal variation effects of plant communities on
761 soil erosion in semiarid grasslands in the Loess Plateau of China, *Catena*, v. 194, 104743–,
762 <https://doi.org/10.1016/j.catena.2020.104743>, 2020.
- 763 Howard, A. D.: A detachment-limited model of drainage basin evolution, *Water Resour. Res.* V 30, 2261–2285, 1994.
- 764 Huang, S., Tang, L., Hupy, J. P., Wang, Y., and Shao, G.: A commentary review on the use of normalized difference
765 vegetation index (NDVI) in the era of popular remote sensing, *J. For. Res.*, 32, 1–6, <https://doi.org/10.1007/s11676-020-01155-1>, 2021.
- 767 Huete, A., Didan, K., Miura, T., Rodriguez, E. P., Gao, X., and Ferreira, L. G.: Overview of the radiometric and biophysical
768 performance of the MODIS vegetation indices, *Remote Sens. Environ.*, 83, 195–213, [https://doi.org/10.1016/S0034-4257\(02\)00096-2](https://doi.org/10.1016/S0034-4257(02)00096-2), 2002.

- 770 Istanbuluoglu, E.: Vegetation-modulated landscape evolution: Effects of vegetation on landscape processes, drainage
771 density, and topography, *J. Geophys. Res.*, 110, <https://doi.org/10.1029/2004jf000249>, 2005.
- 772 Istanbuluoglu, E. and Bras, R. L.: On the dynamics of soil moisture, vegetation, and erosion: Implications of climate
773 variability and change, *Water Resour. Res.*, 42, 2006.
- 774 Johnstone, S. A. and Hilley, G. E.: Lithologic control on the form of soil-mantled hillslopes, *Geology*, 43, 83–86,
775 <https://doi.org/10.1130/G36052.1>, 2014.
- 776 Julien, P. Y., Saghafian, B., and Ogden, F. L.: RASTER-BASED HYDROLOGIC MODELING OF SPATIALLY-VARIED
777 SURFACE RUNOFF1, JAWRA *J. Am. Water Resour. Assoc.*, 31, 523–536, <https://doi.org/10.1111/j.1752-1688.1995.tb04039.x>, 1995.
- 779 Langbein, W. B. and Schumm, S. A.: Yield of sediment in relation to mean annual precipitation, *Eos Trans. Am. Geophys.*
780 *Union*, 39, 1076–1084, <https://doi.org/10.1029/TR039i006p01076>, 1958.
- 781 Leyland, J., Hackney, C. R., Darby, S. E., Parsons, D. R., Best, J. L., Nicholas, A. P., Aalto, R., and Lague, D.: Extreme
782 flood-driven fluvial bank erosion and sediment loads: direct process measurements using integrated Mobile Laser Scanning
783 (MLS) and hydro-acoustic techniques: Direct measurement of flood-driven erosion using MLS and MBES, *Earth Surf.*
784 *Process. Landf.*, 42, 334–346, <https://doi.org/10.1002/esp.4078>, 2016.
- 785 Melnick, D.: Rise of the central Andean coast by earthquakes straddling the Moho, *Nat. Geosci.*, 9, 401–407,
786 <https://doi.org/10.1038/ngeo2683>, 2016.
- 787 Melnick, D., Bookhagen, B., Strecker, M. R., and Echtler, H. P.: Segmentation of megathrust rupture zones from fore-arc
788 deformation patterns over hundreds to millions of years, Arauco peninsula, Chile: EARTHQUAKE SEGMENTATION AT
789 ARAUCO, *J. Geophys. Res. Solid Earth*, 114, <https://doi.org/10.1029/2008JB005788>, 2009.
- 790 Mosaffaie, J., Ekhtesasi, M. R., Dastorani, M. T., Azimzadeh, H. R., and Zare Chahuki, M. A.: Temporal and spatial
791 variations of the water erosion rate, *Arab. J. Geosci.*, 8, 5971–5979, <https://doi.org/10.1007/s12517-014-1628-z>, 2015.
- 792 Oeser, R. A., Stroncik, N., Moskwa, L.-M., Bernhard, N., Schaller, M., Canessa, R., Brink, L. van den, Köster, M., Brucker,
793 E., Stock, S., Fuentes, J. P., Godoy, R., Matus, F. J., Pedraza, R. O., McIntyre, P. O., Paulino, L., Seguel, O., Bader, M. Y.,
794 Boy, J., Dippold, M. A., Ehlers, T. A., Kühn, P., Kuzyakov, Y., Leinweber, P., Scholten, T., Spielvogel, S., Spohn, M.,
795 Übernickel, K., Tielbörger, K., Wagner, D., and Blanckenburg, F. von: Chemistry and microbiology of the Critical Zone
796 along a steep climate and vegetation gradient in the Chilean Coastal Cordillera, *CATENA*, 170, 183–203,
797 <https://doi.org/10.1016/j.catena.2018.06.002>, 2018.
- 798 Rengers, F. K., McGuire, L., Kean, J. W., Staley, D. M., and Hobbey, D. E. J.: Model simulations of flood and debris flow
799 timing in steep catchments after wildfire, *Water Resour. Res.*, 52, 6041–6061, <https://doi.org/10.1002/2015WR018176>,
800 2016.
- 801 Rodell, M., Houser, P. R., Jambor, U., Gottschalck, J., Mitchell, K., Meng, C.-J., Arsenault, K., Cosgrove, B., Radakovich,
802 J., Bosilovich, M., Entin, J. K., Walker, J. P., Lohmann, D., and Toll, D.: The Global Land Data Assimilation System, *Bull.*
803 *Am. Meteorol. Soc.*, 85, 381–394, <https://doi.org/10.1175/BAMS-85-3-381>, 2004.
- 804 Schaller, M. and Ehlers, T. A.: Comparison of soil production, chemical weathering, and physical erosion rates along a
805 climate and ecological gradient (Chile) to global observations, *Earth Surf. Dyn.*, 10, 131–150, <https://doi.org/10.5194/esurf-10-131-2022>, 2022.
- 807 Schaller, M., Ehlers, T. A., Lang, K. A. H., Schmid, M., and Fuentes-Espoz, J. P.: Addressing the contribution of climate and
808 vegetation cover on hillslope denudation, Chilean Coastal Cordillera (26°–38°S), *Earth Planet. Sci. Lett.*, 489, 111–122,
809 <https://doi.org/10.1016/j.epsl.2018.02.026>, 2018.
- 810 Schaller, M., Dal Bo, I., Ehlers, T. A., Klotzsche, A., Drews, R., Fuentes Espoz, J. P., and van der Kruk, J.: Comparison of
811 regolith physical and chemical characteristics with geophysical data along a climate and ecological gradient, Chilean Coastal
812 Cordillera (26 to 38\degree\,S), *SOIL*, 6, 629–647, <https://doi.org/10.5194/soil-6-629-2020>, 2020.
- 813 Schmid, M., Ehlers, T. A., Werner, C., Hickler, T., and Fuentes-Espoz, J.-P.: Effect of changing vegetation and precipitation
814 on denudation – Part 2: Predicted landscape response to transient climate and vegetation cover over millennial to million-
815 year timescales, *Earth Surf. Dyn.*, 6, 859–881, <https://doi.org/10.5194/esurf-6-859-2018>, 2018.

- 816 Sharma and Ehlers: LandLab investigations into the seasonal effects of precipitation and vegetation change on catchment
817 erosion, <https://doi.org/10.5281/zenodo.8033782>, 2023.
- 818 Sharma, H., Ehlers, T. A., Glotzbach, C., Schmid, M., and Tielbörger, K.: Effect of rock uplift and Milankovitch timescale
819 variations in precipitation and vegetation cover on catchment erosion rates, *Earth Surf. Dyn.*, 9, 1045–1072,
820 <https://doi.org/10.5194/esurf-9-1045-2021>, 2021.
- 821 Shobe, C. M., Tucker, G. E., and Barnhart, K. R.: The SPACE 1.0 model: A Landlab component for 2-D calculation of
822 sediment transport, bedrock erosion, and landscape evolution, *Geosci. Model Dev. Discuss.*, 1–38,
823 <https://doi.org/10.5194/gmd-2017-175>, 2017.
- 824 Starke, J., Ehlers, T. A., and Schaller, M.: Latitudinal effect of vegetation on erosion rates identified along western South
825 America, *Science*, 367, 1358–1361, <https://doi.org/10.1126/science.aaz0840>, 2020.
- 826 Steegen, A., Govers, G., Nachtergaele, J., Takken, I., Beuselinck, L., and Poesen, J.: Sediment export by water from an
827 agricultural catchment in the Loam Belt of central Belgium, *Geomorphology*, 33, 25–36, [https://doi.org/10.1016/S0169-555X\(99\)00108-7](https://doi.org/10.1016/S0169-555X(99)00108-7), 2000.
- 829 Stephenson, J., Gallagher, K., and Holmes, C.: A Bayesian approach to calibrating apatite fission track annealing models for
830 laboratory and geological timescales, *Geochim. Cosmochim. Acta*, 70, 5183–5200,
831 <https://doi.org/10.1016/j.gca.2006.07.027>, 2006.
- 832 Suescún, D., Villegas, J. C., León, J. D., Flórez, C. P., García-Leoz, V., and Correa-Londoño, G. A.: Vegetation cover and
833 rainfall seasonality impact nutrient loss via runoff and erosion in the Colombian Andes, *Reg. Environ. Change*, 17, 827–839,
834 <https://doi.org/10.1007/s10113-016-1071-7>, 2017.
- 835 Tucker, G. E. and Bras, R. L.: A stochastic approach to modeling the role of rainfall variability in drainage basin evolution,
836 *Water Resour. Res.*, 36, 1953–1964, <https://doi.org/10.1029/2000wr900065>, 2000.
- 837 Tucker, G. E., Gasparini, N. M., Lancaster, S. T., and Bras, R. L.: *Modeling Floodplain Dynamics and Stratigraphy: Implications for Geoarchaeology*, 1999.
- 839 Übernicketel, K., Ehlers, T. A., Ershadi, M. R., Paulino, L., Fuentes Espoz, J.-P., Maldonado, A., Oses-Pedraza, R., and von
840 Blanckenburg, F.: Time series of meteorological station data in the EarthShape study areas of in the Coastal Cordillera,
841 Chile, <https://doi.org/10.5880/FIDGEO.2020.043>, 2020.
- 842 Van Der Meer, F., Bakker, W., Scholte, K., Skidmore, A., De Jong, S., Clevers, J., Addink, E., and Epema, G.: Spatial scale
843 variations in vegetation indices and above-ground biomass estimates: Implications for MERIS, *Int. J. Remote Sens.*, 22,
844 3381–3396, <https://doi.org/10.1080/01431160152609227>, 2001.
- 845 Wang, L., Zheng, F., Liu, G., Zhang, X. J., Wilson, G. V., Shi, H., and Liu, X.: Seasonal changes of soil erosion and its
846 spatial distribution on a long gentle hillslope in the Chinese Mollisol region, *Int. Soil Water Conserv. Res.*, 9, 394–404,
847 <https://doi.org/10.1016/j.iswcr.2021.02.001>, 2021.
- 848 Wei, W., Chen, L., Zhang, H., and Chen, J.: Effect of rainfall variation and landscape change on runoff and sediment yield
849 from a loess hilly catchment in China, *Environ. Earth Sci.*, 73, 1005–1016, <https://doi.org/10.1007/s12665-014-3451-y>,
850 2015.
- 851 Whipple, K. X. and Tucker, G. E.: Dynamics of the stream-power river incision model: Implications for height limits of
852 mountain ranges, landscape response timescales, and research needs, *J. Geophys. Res. Solid Earth*, 104, 17661–17674,
853 <https://doi.org/10.1029/1999jb900120>, 1999.
- 854 Wulf, H., Bookhagen, B., and Scherler, D.: Seasonal precipitation gradients and their impact on fluvial sediment flux in the
855 Northwest Himalaya, *Geomorphology*, 118, 13–21, <https://doi.org/10.1016/j.geomorph.2009.12.003>, 2010.
- 856 Yetemen, O., Istanbuluoglu, E., Flores-Cervantes, J. H., Vivoni, E. R., and Bras, R. L.: Ecohydrologic role of solar radiation
857 on landscape evolution, *Water Resour. Res.*, 51, 1127–1157, <https://doi.org/10.1002/2014wr016169>, 2015.
- 858 Zhang, S., Li, Z., Hou, X., and Yi, Y.: Impacts on watershed-scale runoff and sediment yield resulting from synergetic
859 changes in climate and vegetation, *Catena*, 179, 129–138, <https://doi.org/10.1016/j.catena.2019.04.007>, 2019.

- 860 Zhang, W., An, S., Xu, Z., Cui, J., and Xu, Q.: The impact of vegetation and soil on runoff regulation in headwater streams
861 on the east Qinghai–Tibet Plateau, China, *Catena*, 87, 182–189, <https://doi.org/10.1016/j.catena.2011.05.020>, 2011.
- 862 Zhang, X., Yu, G. Q., Li, Z. B., and Li, P.: Experimental Study on Slope Runoff, Erosion and Sediment under Different
863 Vegetation Types, *Water Resour. Manag.*, 28, 2415–2433, <https://doi.org/10.1007/s11269-014-0603-5>, 2014.
- 864 Zheng, F. L.: Effect of Vegetation Changes on Soil Erosion on the Loess Plateau1 1Project supported by the Chinese
865 Academy of Sciences (No. KZCX3-SW-422) and the National Natural Science Foundation of China (Nos. 9032001 and
866 40335050)., *Pedosphere*, 16, 420–427, [https://doi.org/10.1016/S1002-0160\(06\)60071-4](https://doi.org/10.1016/S1002-0160(06)60071-4), 2006.
- 867 Ziese, M., Rauthe-Schöch, A., Becker, A., Finger, P., Rustemeier, E., and Schneider, U.: GPCC Full Data Daily Version
868 2020 at 1.0°: Daily Land-Surface Precipitation from Rain-Gauges built on GTS-based and Historic Data: Gridded Daily
869 Totals (2020), https://doi.org/10.5676/DWD_GPCC/FD_D_V2020_100, 2020.

870